D2.1 Ecosystem Functioning Response to Extreme Climate Change-Related Events

Funded by
the European Union

Document Identification			
Related WP	WP4, WP1	Document reference	D2.1
Status	Final	Submissions date	30/6/2026
Related deliverables	-	Dissemination Level	PU
Lead Author	Elnaz Neinavaz (UT/ITC)	Version	1.0
Co-Authors	Anne Gobin (KU Leuven) Jiri Sedlak (VSUO) Karel Charvat (Plan4all) Kristian Bottcher (SYKE) Hongxiao Jin (ULUND)	Reviewers	Bob O'Hara (NTNU) Dmitry Schepaschenko (IIASA)
Keywords	Biodiversity monitoring, EBVs, ECVs, Earth Observation, Land Surface Temperature, Ecosystem Functioning	Website	https://bioclima.net/

This document is issued within the framework and for the purpose of the BioClima project. This project has received funding from the European Union's Horizon-RIA Framework Programme under Grant Agreement No. 101181408. The opinions expressed and arguments employed herein do not necessarily reflect the official views of the European Commission.

Document History			
Version	**Date**	**Editors**	**Changes**
0.1	10/2/2026	UT/ITC	Initial Draft
0.2	29/06/2026	UWB	Reviewed Version
1.0	30/06/2026	UT/ITC	Final Version

Table of Contents

List of Tables

List of Figures

List of Acronyms

Acronym	Description
AI	Artificial Intelligence
AMPL	Seasonal Growth Amplitude
CLMS	Copernicus Land Monitoring Service
EBV	Essential Biodiversity Variable
ECV	Essential Climate Variable
EO	Earth Observation
ECMWF	European Centre for Medium-Range Weather Forecasts
EOSD	End of the Season
EVI	Enhanced Vegetation Index
ET	Evapotranspiration
fAPAR	Absorbed Photosynthetically Active Radiation
fCover	Fractional Vegetation Cover
LENGTH	Length of the Growing Season
HR-VPP	Copernicus High Resolution-Vegetation Phenology and Productivity
ICOS	Integrated Carbon Observation System
LAI	Leaf Area Index
LST	Land Surface Temperature
MODIS	Moderate Resolution Imaging Spectroradiometer
MR-VPP	Medium Resolution Vegetation Phenology and Productivity
NDRE	Normalised Difference Red Edge Index
NDVI	Normalized Difference Vegetation Index
NDWI	Normalised Difference Water Index
PET	Potential Evapotranspiration
PPI	Plant Phenology Index
R	Pearson correlation
R^2	Coefficient of determination
RMSD	Root-Mean-Squared Deviation
RMSE	Root-Mean-Squared Error
rRMSE	Relative Root-Mean-Squared Error
SAVI	Soil-Adjusted Vegetation Index
SPEI	Standardized Precipitation Evapotranspiration Index
saSPEI	Snow-adjusted Standardized Precipitation Evapotranspiration Index
SOSD	Start of the Season

Acronym	Description
TPROD	Total Productivity
UAV	Unmanned Aerial Vehicles

Executive Summary

This deliverable investigates the impacts of climate change-related extreme events across a portfolio of case studies located in different regions of Europe, including Northern Finland, Czechia, the European Arctic, Crete, and northern Belgium. These case studies represent diverse ecological settings, climate-related stressors, temporal requirements, Earth observation (EO) data sources, and expected outputs. The analyses are based on Essential Biodiversity Variables (EBVs) and Essential Climate Variables (ECVs), which provide a harmonised framework for assessing ecosystem responses to climate extremes. While Deliverable D2.1 presents the comprehensive scientific reports, including the objectives, methodologies, analyses, and findings for each case study, the present deliverable focuses on the EO-derived products generated from these activities and their dissemination.

A key contribution of this deliverable is the use of EO data and EO-derived products to retrieve and analyse EBVs and ECVs. Where appropriate, existing EO-based EBV and ECV products were integrated into the analyses, while in other cases, new EO-derived products were generated specifically for the project. This approach enables consistent, spatially explicit, and repeatable monitoring of ecosystem responses to climate change-related extreme events across diverse environmental settings.

The five case studies address different ecosystems and climate-related hazards, including drought, heatwaves, and other extreme events. Consequently, different EO sensors, datasets, and derived products were selected according to the spatial and temporal requirements of each study. These include satellite missions such as Sentinel-2, Landsat, UAV imagery, and complementary climate and field observations. Appropriate processing workflows and analytical methods were applied to derive relevant EBVs and ECVs, ensuring that the selected variables accurately represent ecosystem functioning and environmental conditions.

By integrating EO-derived EBVs, ECVs, and supporting field observations, this deliverable contributes to a better understanding of how ecosystem functions respond to climate change-related extreme events. The generated products provide valuable information for ecosystem monitoring, support future biodiversity and climate assessments, and demonstrate the potential of EO technologies for operational monitoring within the BioClima project.

This deliverable will make a significant contribution to both WP1 and WP4. It provides a cross-work-package methodological foundation by establishing harmonised approaches for deriving and applying EBVs and ECVs from EO data. Rather than serving as a stand-alone modelling report, the deliverable presents a consistent methodological framework that supports the integration of EO-based products across the BioClima project. The generated products, processing workflows, and dissemination strategy will facilitate subsequent analyses, ecosystem assessments, and decision-support activities within

WP4, while also contributing to the project's overall data integration and methodological objectives in WP1.

1. Introduction

Climate change is increasingly altering the structure, composition, and functioning of ecosystems worldwide through the growing frequency and intensity of extreme events such as droughts, heatwaves, floods, storms, and wildfires. These disturbances can substantially affect ecosystem processes, including primary productivity, phenology, nutrient cycling, carbon sequestration, and water regulation, thereby reducing ecosystem resilience and the provision of essential ecosystem services. Monitoring ecosystem functioning is therefore fundamental for understanding how ecosystems respond to environmental change, assessing their vulnerability and resilience, and supporting evidence-based conservation and management strategies.

Traditional field-based ecological monitoring provides detailed and accurate information but is often spatially limited, labour-intensive, and difficult to maintain over large areas or long time periods. As climate change impacts occur across multiple spatial and temporal scales, there is an increasing need for harmonised monitoring approaches that provide consistent, repeatable, and comparable observations across ecosystems and regions. EBVs have been developed to address this need by providing a standardized framework for monitoring key dimensions of biodiversity change. EBVs bridge the gap between raw biodiversity observations and policy-relevant biodiversity indicators by attempting to capture fundamental biological attributes, including species populations, community composition, ecosystem structure, and ecosystem functioning. Among these, ecosystem functioning EBVs—including vegetation productivity, phenology, and vegetation activity—are particularly valuable because they provide measurable indicators of ecosystem responses to environmental change and climate-related disturbances.

Similarly, ECVs provide standardized observations of the physical climate system that are required for climate monitoring, modelling, and adaptation planning. Variables such as land surface temperature, soil moisture, precipitation, and radiation describe the environmental conditions that directly influence ecosystem processes and biodiversity patterns. Integrating EBVs with ECVs enables a comprehensive assessment of ecosystem responses by linking changes in biodiversity and ecosystem functioning to their underlying climatic drivers.

EO technologies have become indispensable for deriving both EBVs and ECVs at regional to global scales. Satellite missions such as Sentinel and Landsat, together with airborne platforms and unmanned aerial vehicles (UAVs), provide continuous, spatially explicit, and long-term observations of vegetation, land surface temperature, moisture conditions, and other environmental characteristics. Advances in EO data processing, cloud computing, and open-access satellite archives now enable the routine generation of standardized biodiversity and climate products with high temporal frequency and spatial resolution. These capabilities allow researchers to detect ecosystem disturbances, quantify recovery following extreme events, monitor seasonal dynamics, and evaluate long-term environmental trends in a consistent and reproducible manner.

Within the BioClima project, EO-derived EBVs and ECVs provide the methodological foundation for assessing ecosystem responses to climate change-related extreme events across diverse European ecosystems. By integrating satellite observations with field measurements and ancillary environmental data, the project develops harmonised products that support biodiversity monitoring, climate impact assessment, and ecosystem resilience analysis. The products generated by this work contribute to a consistent framework for evaluating ecosystem functioning across multiple case studies and support future applications in biodiversity conservation, climate adaptation, and environmental decision-making.

2. Case study 1: Satellite-based Indicators of Vegetation Response to Hydroclimatic Variability Using EBV and ECV

2.1 Introduction

Climate variability is a key driver of ecosystem dynamics, influencing vegetation phenology, productivity, and overall ecosystem functioning through changes in temperature and water availability. ECVs, such as temperature and precipitation, shape these processes, while advances in EO enable consistent, large-scale monitoring of vegetation responses through EBVs, including phenological and productivity indicators. Within this context, the ULUND team in WP2.1 aims to develop spatially explicit, EO-based indicators that link ECVs to EBVs, providing a harmonised framework for assessing ecosystem responses to climatic variability and supporting biodiversity–climate analyses across regions. In addition, soil moisture is an ECV that plays a key role in ecosystems and the energy, water, and carbon cycles. Two characteristic soil moisture variables are commonly used, each important for certain applications. Specifically, the surface soil moisture (the top 0-5 cm in depth) and the root zone soil moisture (0-100cm depth). Accurate estimation of soil moisture (surface and root zone) is important for many applications in the BioClima project. Thus, the ULUND team also evaluated multiple existing gridded surface- and root-zone soil-moisture products in Europe using recently available measurements from the Integrated Carbon Observation System (ICOS).

2.2 Objectives

The objectives of this case study are to develop a robust, EO-based framework for assessing vegetation responses to climate variability. Specifically, the study aims to:

(i) Derive consistent and scalable indicators of vegetation dynamics, including phenological metrics and productivity proxies, from satellite time series;

(ii) Quantify the relationships between key ECVs, such as temperature and precipitation, and vegetation responses captured through EBVs

(iii) Generate spatially explicit metrics that enable the assessment of biodiversity–climate interactions and support harmonized monitoring of ecosystem functioning across regions.

Not directly integrated into the three objectives, we have a fourth objective to achieve by our ULUND team, which is

(iv) evaluate multiple existing gridded surface soil moisture products and root zone soil moisture products in Europe using the recently available measurements from ICOS (Integrated Carbon Observation System).

2.3Study Area

The study covers Europe and northern high-latitude regions, encompassing a wide range of climatic and ecological conditions, from temperate and boreal ecosystems to more water-limited environments. This spatial extent captures strong gradients in temperature, precipitation, and seasonality, as well as varying exposure to drought and hydroclimatic variability. Such diversity provides a suitable context for analysing vegetation responses across different ecosystem types and climate regimes, thereby supporting the development and evaluation of EO-based indicators that link climate variability to ecosystem dynamics.

2.4 Data

- ***Data Sources Used***

Satellite-based EO data were used to derive vegetation dynamics, including Sentinel-2 surface reflectance products and Moderate Resolution Imaging Spectroradiometer (MODIS) time series, as well as Copernicus Land Monitoring Service (CLMS) products such as the Medium Resolution Vegetation Phenology and Productivity (MR-VPP). Climate data were obtained from reanalysis and merged datasets, including ERA5-Land for temperature and precipitation and MSWEP for precipitation. In addition, drought indicators were derived from these datasets, including the Standardized Precipitation Evapotranspiration Index (SPEI) and a snow-adjusted SPEI (saSPEI) developed to better represent hydroclimatic conditions in northern high-latitude regions. The CLMS MRVPP dataset used in this contribution is publicly available via Zenodo at https://zenodo.org/records/19653683. The SPEI drought data are disseminated through the Lund University Global Drought Dataset (LUGD), 1981–2025, available at https://zenodo.org/records/18985819. The saSPEI data will be available on Zenodo after validation.

- ***Data Type(s)***

The analysis integrates multi-source geospatial time series data, including satellite-derived vegetation indices and phenological metrics, gridded climate variables (temperature and precipitation), and derived drought indices. These datasets are harmonised in space and time to enable consistent analysis of vegetation–climate interactions.

- ***EBVs Applied***

Vegetation-related EBVs were derived from EO time series, with a focus on phenology and productivity. Phenological metrics include the start of the season (SOSD), the end of the season (EOSD), and the length of the growing season (LENGTH). Productivity indicators include the Plant Phenology Index (PPI) and integrated productivity metrics, such as seasonal total productivity (TPROD) and seasonal growth amplitude (AMPL), which represent vegetation activity and ecosystem functioning.

- ***ECVs Applied***

Key climate drivers were characterised using ECVs, including near-surface air temperature (ERA5-Land T2m) and precipitation (ERA5-Land and MSWEP). These variables were further used to derive drought indicators, including SPEI and saSPEI, to capture water availability and hydroclimatic stress conditions influencing vegetation dynamics.

2.4.1 Evaluated Multiple Gridded Soil Moisture Products

Eight widely used gridded surface soil moisture products were evaluated (listed in Table 1), and seven widely used root-zone soil moisture products using ICOS measurements. The ICOS is a European collaboration and infrastructure to monitor the carbon cycle. ICOS hosts atmospheric, ocean, and ecosystem stations. This study uses data from the ecosystem stations, of which there are currently 87. However, many of these stations do not have coverage during 2020 and 2021. Instead, only 38 ICOS stations provided soil moisture data for most of the study period and were therefore used to evaluate eight surface soil moisture products. All ICOS data are available at the ICOS Carbon Portal https://www.data.icos-cp.eu.

For root-zone soil moisture, measurements are more difficult to obtain at all considered depths. Despite existing recommendations for soil measurement depths, stations may deviate from them for various reasons. As a result, not all measurements reach a depth of 1m, as required for this evaluation. Stations with measurements at 5 different depths were generally found to meet the requirements and reach the root zone depth. A data-filtering analysis showed that a maximum of 25 stations overlapped for at least two years during the same period and were therefore considered eligible for use in this study. The 2-year overlap for these 25 stations was 2022-2023.

Table 1. An overview of eight gridded surface soil moisture products.

Gridded Product	Grid Resolution	Temporal Coverage	Coverage	Sampling Depth (cm)	Frequency (GHz)
Sentinel-1	1 km	April 2014 – present	Europe	0-5	5.405 (C)

Gridded Product	Grid Resolution	Temporal Coverage	Coverage	Sampling Depth (cm)	Frequency (GHz)
SMAP L3E	9 km	March 2015 – present	Global	0-5	1.41 (L)
SMAP L4	9 km	March 2015 – present	Global	0-5	1.41 (L)
SMOS L4	1 km	June-2010 – present	Europe	0-5	1.4 (L)
ASCAT	12.5 km	January 2019 – present	Global	0-5	5.255 (C)
ESA CCI SM	0.25°	January 1978 - December 2021	Global	0-5	Various
ERA5-Land	0.1°	January 1950 – present	Global	0-7	-
GLDAS Noah	0.25°	January 2000 - present	Global	0-10	-

Table 2. An overview of seven gridded root zone soil moisture products.

Product	Spatial Resolution	Temporal Resolution	Depth (cm)	Time period
ERA5-Land	0.1° x 0.1°	Hourly	0-289	1950-Present
GLDAS-NOAH v2.1	0.25° x 0.25	3-Hourly	0-200	2000-Present
SMAP-L4	9km x 9km	3-Hourly	0-100	2015-Present
SMOS-L4	25km x 25km	Daily	0-100	2010-Present
NCEP-R2	2.5° x 2.5°	6-Hourly	0-200	1978-Present
MERRA-2	0.5° x 0.625°	Hourly	0-100	1980-Present
GLEAM 4.2a	0.1° x 0.1°	Daily	0-100*	1980-2023

2.5 Methodology

The methodology integrates multi-source EO and climate data to derive vegetation indicators and assess their relationship with climatic variability. First, EO time series from Sentinel-2 and MODIS were pre-processed using a harmonised processing chain, including quality filtering, Bidirectional Reflectance Distribution Function normalisation, and temporal compositing to ensure consistency across sensors and time. Further, vegetation dynamics were characterised using time-series analysis with established approaches, including TIMESAT, enabling the extraction of phenological metrics such as the start and end of the season, as well as productivity-related indicators derived from vegetation indices. The official TIMESAT repository hub is available at https://github.com/TIMESAT. In addition, EBVs, including phenology and productivity metrics, were systematically derived at the pixel level to provide spatially explicit representations of ecosystem functioning. Finally, these EBVs were analysed in relation to ECVs, including temperature, precipitation, and drought indices (SPEI and snow-adjusted SPEI), using statistical approaches such as correlation analysis, anomaly detection, and trend assessment. This framework enables the quantification of vegetation responses to climate variability across different spatial and temporal scales.

Evaluation of gridded soil moisture products was performed following the common practices in the publications. Widely used metrics were calculated to assess product accuracy against ground measurements from ICOS stations. They are the linear Pearson correlation (R), the Root-Mean-Squared Deviation (RMSD) or the Root-Mean-Squared Error (RMSE), and the bias. It is also recommended to use scaled versions of the metrics when comparing absolute soil moisture data, i.e., after removing inherent product bias. Thus, for RMSD, the unbiased RMSD (ubRMSD) or ubRMSE was used instead. In this context, RMSD and RMSE are exchangeable, and ubRMSD and ubRMSE are exchangeable as both are used in different publications.

2.6 Results

The derived EO-based indicators reveal clear spatial patterns in vegetation dynamics and their response to climatic variability across the study domain. Phenological metrics, including SOSD, EOSD, and LENGTH, show strong geographic gradients consistent with temperature and seasonal regimes, with earlier onset and longer growing seasons in warmer regions and delayed phenology in higher latitudes. Productivity indicators (TPROD and AMPL) exhibit spatial variability that aligns with water availability, highlighting reduced vegetation productivity in drought-prone regions and enhanced productivity in areas with favourable hydroclimatic conditions. Drought indicators (SPEI and snow-adjusted SPEI) capture the spatial distribution of hydroclimatic stress, particularly in northern and water-limited regions where snow dynamics influence water availability. Spatial comparison of EBVs and ECVs indicates consistent relationships between vegetation dynamics and climate variability. Productivity metrics show strong correspondence with drought conditions, with reduced productivity observed under negative SPEI/saSPEI anomalies. These patterns are further supported by correlation analyses, which demonstrate spatially coherent links between vegetation activity and hydroclimatic drivers.

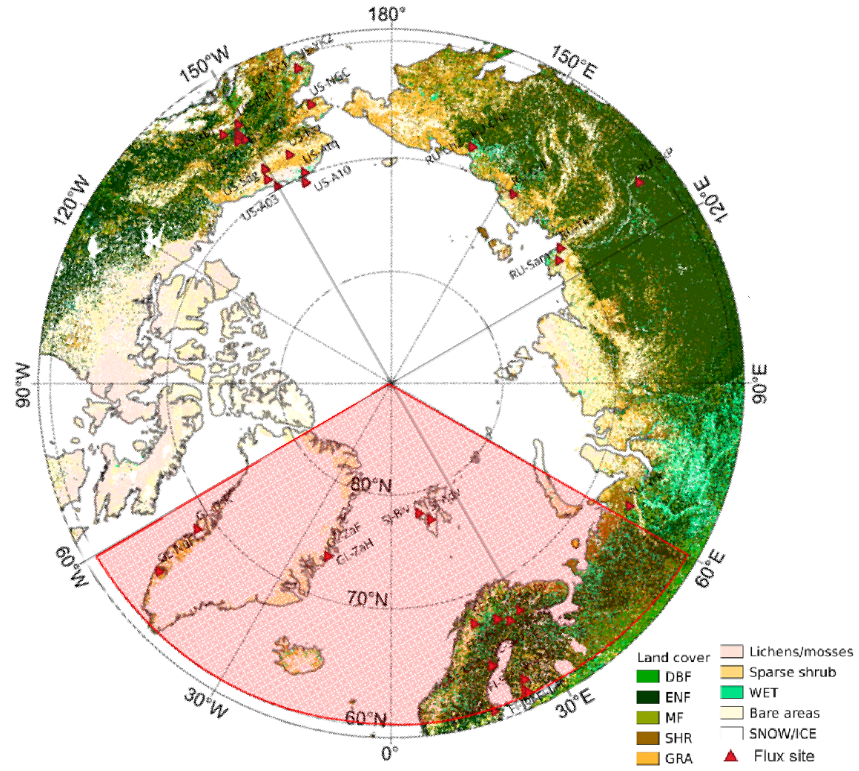

Figure 1. Land cover map and the study area (shaded area)

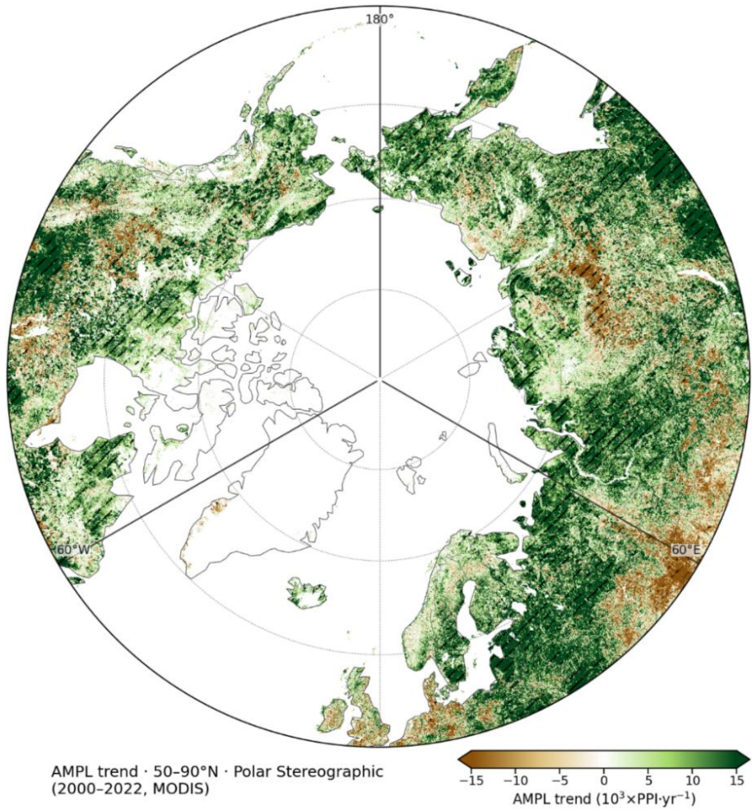

Figure 2. Trend of growing season amplitude (AMPL) using MODIS data, indicating green or browning occurrence during 2000-2022

The drought regime has totally changed in Abisko.

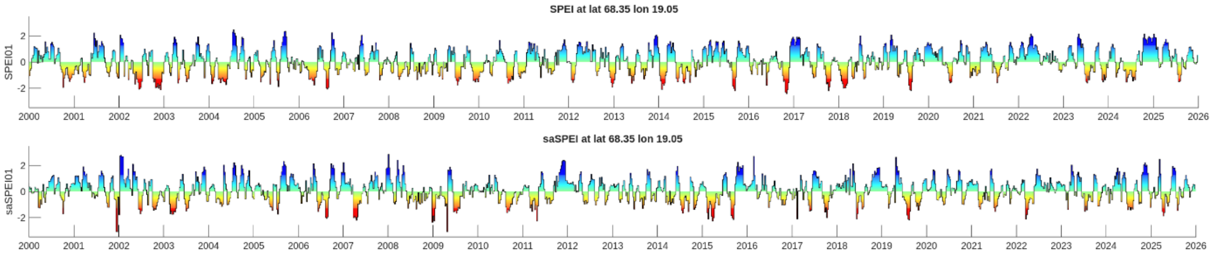

Figure 3. Time series of SPEI and saSPEI in Abisko, sub-Arctic Sweden.

2.6.1 Evaluation of Soil Moisture Products

Figure 4 shows the evaluation results of 8 gridded surface soil moisture products against measurements from 38 ICOS stations during 2020-2021. Overall, the top three products with increasing error ubRMSD are SMAP L4, ESA-CCI soil moisture, and ERA5-Land. The top three products by decreasing R are the SMAP L4, ER5-Land, and ESA-CCI soil moisture.

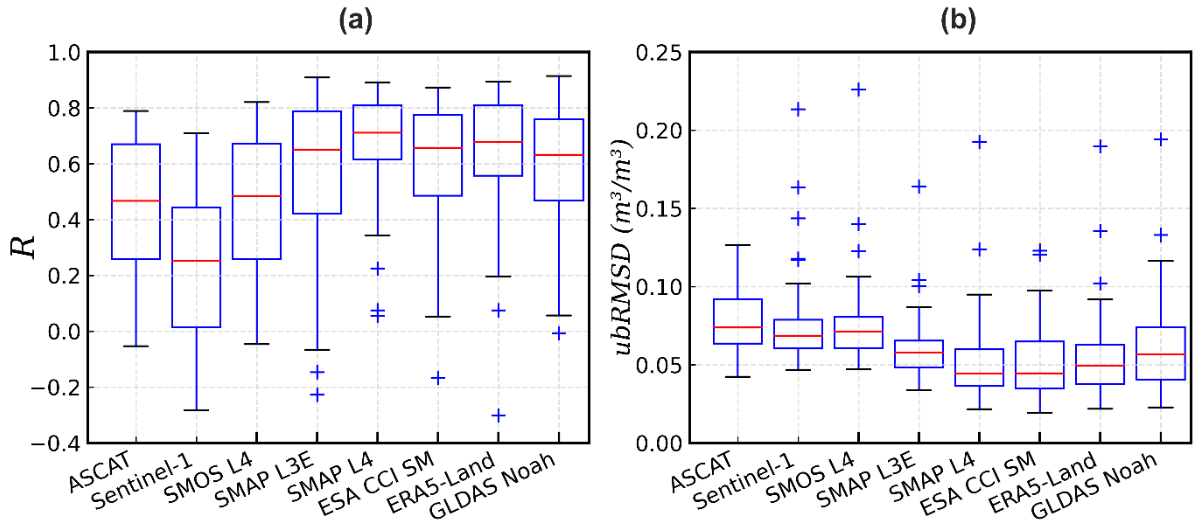

Figure 4. The evaluation metrics R9a) and ubRMSD (b) for each soil moisture product at the ICOS stations were calculated based on absolute soil moisture and non-collected dates between products.

Figure 5 presents the overall accuracy of 7 evaluated root zone soil moisture products against measurements from 25 ICOS stations during 2022-2023. The results show that the top three products by increasing error (ubRMSE) are MERRA2, SMAP, and GLEAM42. The top three products with decreasing R are ERA5-Land, MERRA2, and NOAH. In contrast, the surface soil moisture products tend to be more consistent across the performance metrics; the same top three products are identified using R or ubRMSD. However, the ranking of root zone soil moisture products varies depending on the metric used.

(a)

(b)

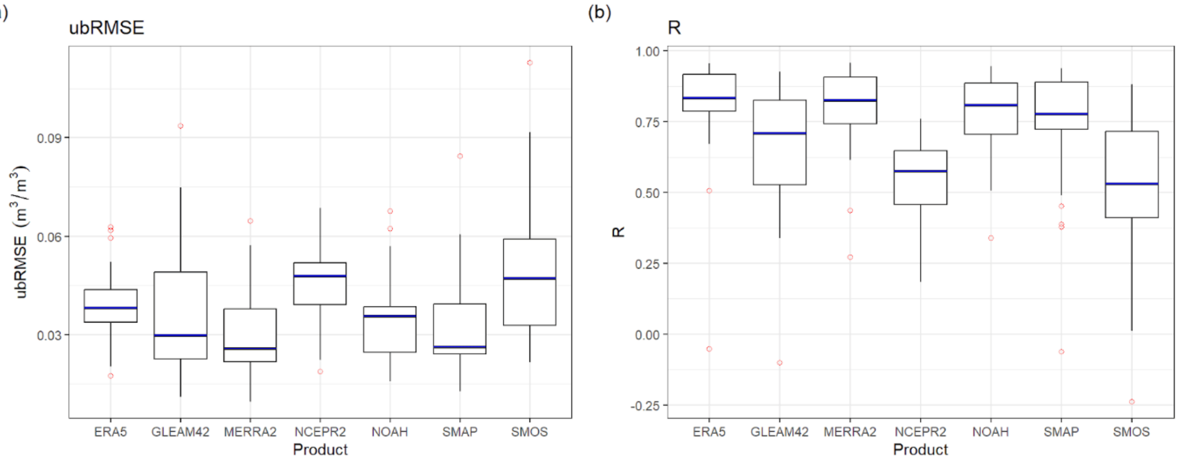

Figure 5. Summary of the performance metrics (a) ubRMSE and (b) Pearson correlation coefficient for the seven products in comparison to in-situ measurements from ICOS for the time period 2022-2023. The median is shown in blue, with outliers shown as red points.

2.7Distribution of the Products

The ULUND contribution generated and/or used EO-derived vegetation phenology, productivity, and drought-related products that are made publicly available through open repositories. The main dissemination routes are Zenodo for data products and GitHub for the TIMESAT software framework used in vegetation time-series processing.

Table 3. The products generated in this case study.

Product/Resource	Description	Access link
CLMS Medium Resolution Vegetation Phenology and Productivity (MRVPP) dataset, Version 6.0	Medium-resolution vegetation phenology and productivity dataset, including phenological and productivity metrics such as SOSD, EOSD, LENGTH, AMPL, and TPROD.	https://zenodo.org/records/19653683
Lund University Global Drought Dataset (LUGD), 1981–2025	Weekly 0.1° SPEI dataset for the Northern Hemisphere, with accumulation timescales from 1 week to 48 months. This dataset supports drought and hydroclimatic stress analyses, including SPEI-	https://zenodo.org/records/18985819

Product/Resource	Description	Access link
	based interpretation of vegetation responses.	
Snow-adjusted SPEI ((LUGD saSPEI, 1981–2025)	Will be uploaded to Zenodo after full validation.	TBD
TIMESAT official GitHub organization	Official repository hub for TIMESAT, the software framework used for satellite vegetation time-series processing and extraction of phenology and productivity metrics.	https://github.com/TIMESAT

These resources support public dissemination and reuse of the vegetation phenology, productivity, and drought-related outputs used in the ULUND T2.1 contribution. The datasets are openly accessible via Zenodo, while the TIMESAT software framework is disseminated through the official GitHub organization.

3. Case study 2: Investigating the impact of Climate Change on Ecosystem Functioning Using EBV and ECV in Northern Finland

3.1 Introduction

Work in WP2.1 supports the development and execution of the Northern Finland case study in Task 4.1, with the goal of optimising decision-making by integrating modelled carbon balance estimates and EO of natural habitats to identify areas with high biodiversity and carbon sequestration potential. The case study aims to improve our understanding of how ecosystem functions and services (carbon sequestration and timber production) are associated with different habitats and how these are affected by climate change and land-use processes. Task 2.1 contributes to this by collecting and analysing remote sensing data products that describe EBVs of ecosystem phenology and productivity, as well as ECVs, with a focus on snow cover.

3.2 Objectives

- Analyse changes in snow cover, phenology and productivity in northern Finland
- Test the Copernicus HR-VPP productivity metric for describing productivity in different habitats in the study area.

3.3 Study Area

The study area is located in northern Finland, covering about three million. Hectares. Most of the study area is protected and part of the Natura 2000 network. The main Natura 2000 habitat types include Western taiga, Nordic subalpine/subarctic forest (mountain birch forest), Alpine and boreal heath, and different mire types. The area is characterised by a subarctic climate with cool summers and precipitation distributed throughout the year. Rapid climate warming and changes in precipitation and snow mass are evident in the region (e.g., Pulliainen et al. (2020), Rantanen et al. (2022)). Climate warming causes the advancement of the coniferous tree line, increased shrub growth, and the melting of palsa mires. The warming favours insect mass outbreaks that cause damage to mountain birch forests. Currently, more than 1/3 of fell habitats are endangered by climate change, intensive reindeer grazing, and their combined effects (Tammilehto et al., 2024).

3.4 Data

- ***Data Sources Used:***

Satellite-based data products from the MODIS and Landsat time series were used to assess long-term trends in the study region, alongside climate observations. The

Copernicus High Resolution-Vegetation Phenology and Productivity (HR-VPP) product was applied together with in situ observations (inventory classes, Natura 2000 habitat types, and habitat quality). Data sources are described in more detail below.

MODIS time series. The start-of-season (greening-up) and snowmelt-off dates were determined from MODIS satellite observations for the period 2001 to 2023 using methods described in Böttcher et al. 2016 and Metsämäki et al. 2018. The greening date describes the day when deciduous trees unfold their leaves in spring. It is provided at a spatial resolution of 5 km x 5 km for Finland. The snowmelt-off date was determined from the Copernicus Pan-European Snow Cover Extent product, with a spatial resolution of 500 × 500 m.

Landsat satellite time-series. Landsat time series of annual summer reflectance mosaics and the Normalized Difference Vegetation Index (NDVI) were processed from the Landsat Collection 2 Level 2 Surface Reflectance data provided by USGS1. Data are based on instruments onboard the Landsat-5, -7, -8, and -9 satellites and cover the years 1984-2024. Yearly mosaicking was based on the maximum NDVI value.

In situ observations. Field data were available from 4,500 plots over three field seasons (2020-2022) (Tammilehto et al., 2024). For each field plot, habitat information was assessed within a 10-meter circular plot. The information from field sample plots aligns with the protected area information system used by Metsähallitus to manage conservation areas in Finland. Here, we use information on Natura 2000 habitat types and the inventory classes (Finnish national system).

Copernicus HR-VPP. The Copernicus High-Resolution Vegetation Phenology and Productivity product provides phenology and productivity metrics at a pan-European level from Sentinel-2 data starting in 2017, with a spatial resolution of 10 m. In this analysis, we utilised the annual total productivity metric (TPROD) for the period 2020 to 2023. Data with quality class 0 (no data), 1 (no season detected), and 2 (filled observations) were excluded from the analysis.

Climate data. Bioclimatic variables derived from gridded climate data (1961-2020) covering Finland at a spatial resolution of 1 x 1 km were utilised. The data set is based on spatial interpolation of weather station data, incorporating external predictors such as elevation, lake coverage, proximity to the sea, latitude and longitude, and relative elevation (Aalto et al., 2023).

- ***Data Type(s):***

The analyses used in situ, satellite, and gridded climate observations. ***EBVs Applied:***

- o Ecosystem phenology: The start-of-season (greening-up) of vegetation was determined from MODIS time series using the methodology described in Böttcher et al. (2016).

- Ecosystem productivity: The maximum summer NDVI derived from Landsat time series and the Copernicus HR-VPP TPROD metric were used as a proxy for primary productivity.
  - ***ECVs Applied:***
- Snow cover: The snowmelt-off date was determined from Fractional Snow Cover for Pan-Europe (Copernicus Service Snow and Land Ice) from MODIS time series using the methodology by Metsämäki et al. (2018).
- Snow thickness, melt-day, and snow days based on daily gridded climate data (Aalto et al., 2023).

3.5Methodology

Trend analysis. Trends in time series of summer NDVI, vegetation greening, and snow variables were analysed using the non-parametric Mann–Kendall test for monotonic trends, including Sen's slope estimation. Analyses were performed at the pixel level for the period 2001–2020. This period was selected because it is consistently covered by both satellite observations and gridded climate data at an appropriate spatial resolution.

Statistical analysis of field data. To assess differences in TPROD among habitat types, HR-VPP TPROD values were averaged over the period 2020–2023. Summary statistics were then calculated for each habitat type based on both Natura 2000 classifications and field inventory classes.

3.6Results

Trends in start-of-season and snow cover. Trends in the start of the growing season (green-up), derived from MODIS satellite observations, were not significant during the period 2001–2020 (Figure 6b). However, the spatial patterns indicate earlier green-up in open vegetation types and delayed green-up in forested areas (Figure 6a). In contrast, significant trends toward later snowmelt were observed across most of northern Finland, based on both satellite and climate data for the same period (Figures 6c, 6d, 7a, 7b). Precipitation has increased in recent decades in northern Finland, leading to a significant increase in snow cover thickness and in the number of snow-covered days across large parts of the study area (Figure 2 c-f).

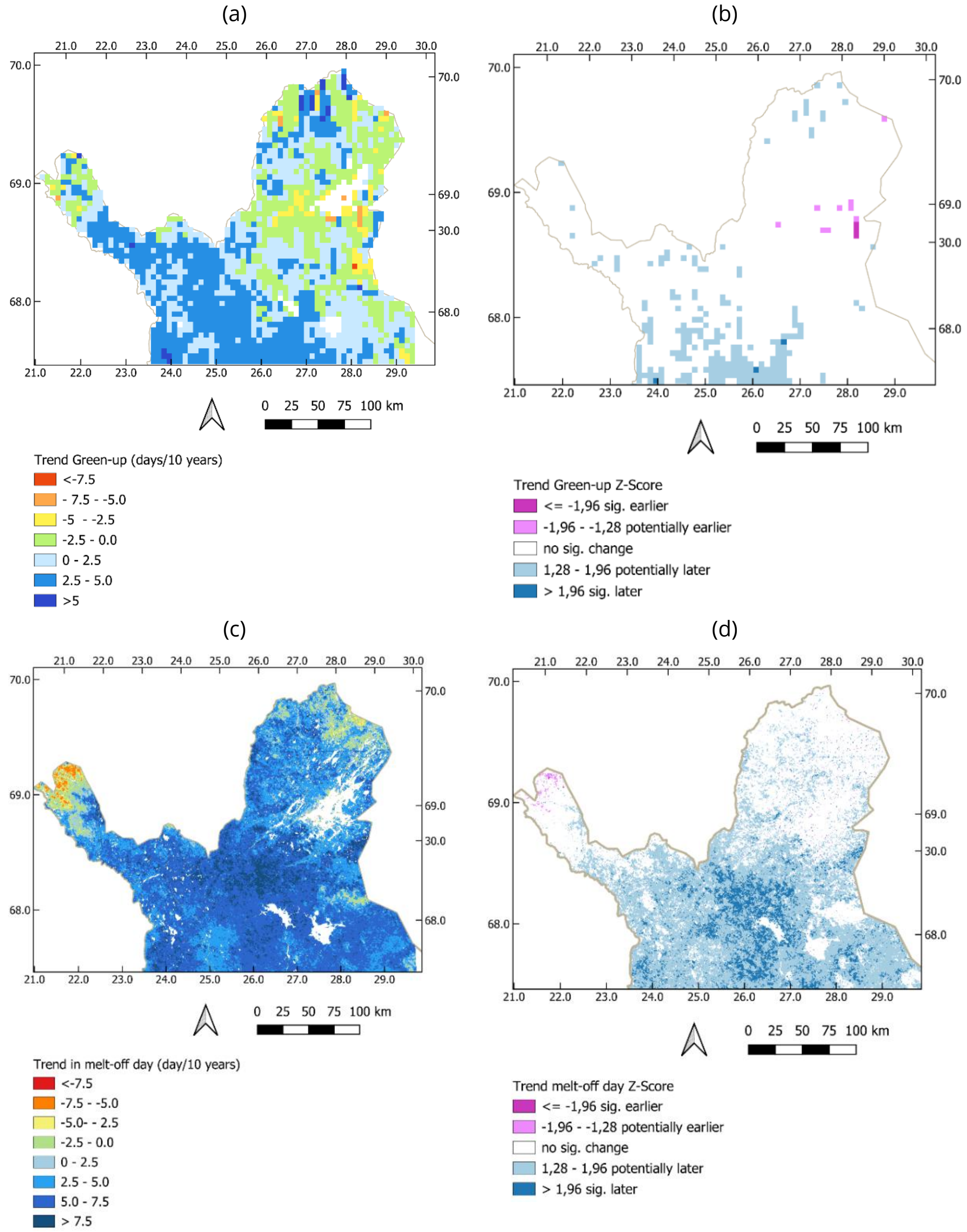

Figure 6. Trends in the start of the season of deciduous vegetation (green-up) (a) and snowmelt-off day (c) from satellite observations and trend significance (Z-score, b, d) in Northern Finland

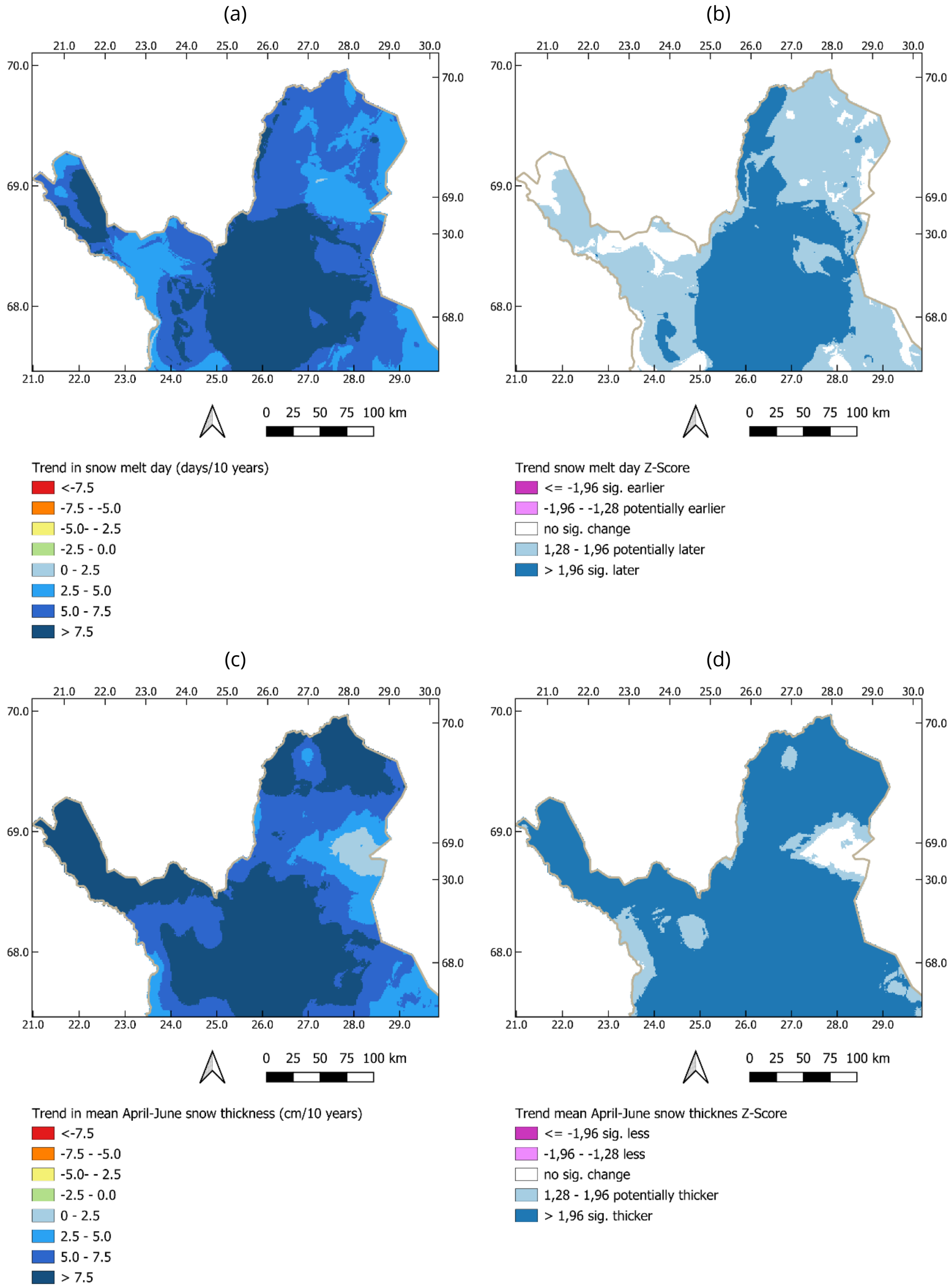
(a)
(b)
0 25 50 75 100 km
Trend in snow melt day (days/10 years)
<-7.5
-7.5 - -5.0
-5.0- - 2.5
-2.5 - 0.0
0 - 2.5
2.5 - 5.0
5.0 - 7.5
> 7.5
Trend snow melt day Z-Score
<= -1,96 sig. earlier
-1,96 - -1,28 potentially earlier
no sig. change
1,28 - 1,96 potentially later
> 1,96 sig. later
(c)
(d)
Trend in mean April-June snow thickness (cm/10 years)
<-7.5
-7.5 - -5.0
-5.0- - 2.5
-2.5 - 0.0
0 - 2.5
2.5 - 5.0
5.0 - 7.5
> 7.5
Trend mean April-June snow thicknes Z-Score
<= -1,96 sig. less
-1,96 - -1,28 less
no sig. change
1,28 - 1,96 potentially thicker
> 1,96 sig. thicker

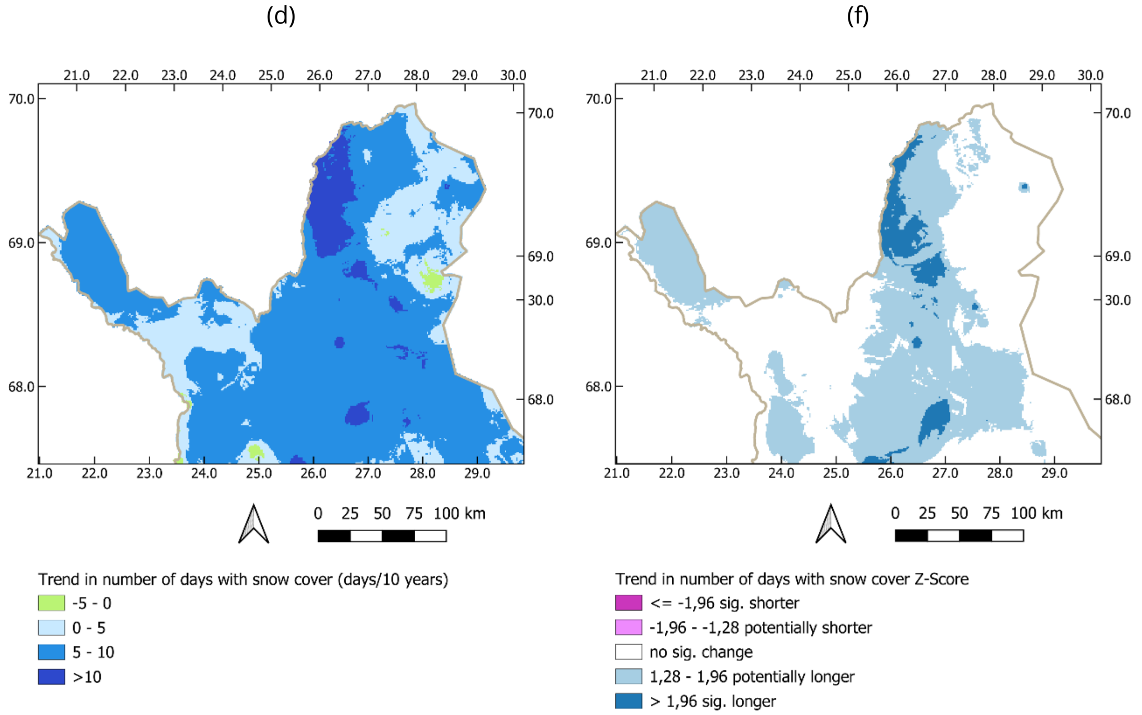

Figure 7. Trends in snowmelt day (a), mean April-June snow thickness (c), and number of days with snow cover (d) and trend significance (Z-score, b, d, and f) from gridded climate data in Northern Finland for the period 2001-2020.

Trends in summer NDVI. Large parts of the study area in northern Lapland showed significant positive trends in maximum summer NDVI from 2001 to 2020 (Figure 8). Significant negative trends were observed in areas with mining activities, forest cuttings, and insect mass outbreaks. The observed trends in Landsat NDVI require further validation. The completeness and quality of the annual reflectance mosaics depend on image availability and on technical factors that affect image quality, such as cloud cover and striping caused by the Landsat 7 sensor failure. Atmospheric effects remained visible in the reflectance mosaics, and some cloud and cloud shadow areas were not correctly detected, introducing errors into the maximum NDVI composites. Further improvements in cloud and shadow masking of Landsat reflectance data are therefore needed.

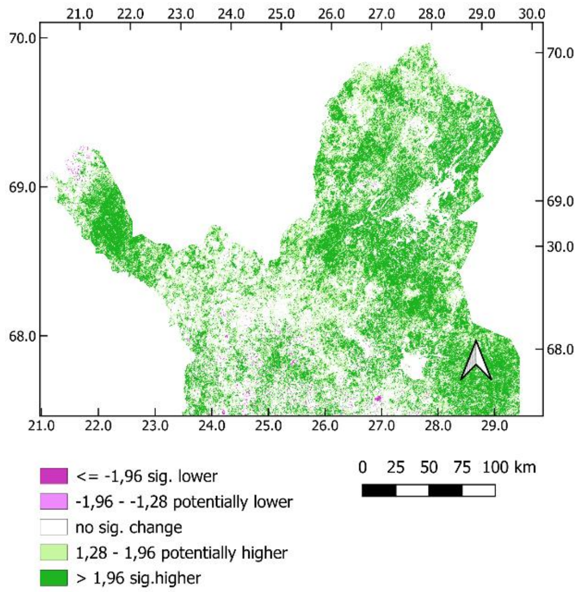

Figure 8. Trends (Z-score) in maximum summer NDVI derived from Landsat for the period 2001 to 2020.

Productivity for habitat types. The distribution of TPROD in the study area is shown alongside the distribution of Natura 2000 habitat types in Figure 4. Higher productivity is observed in forested areas than in alpine, boreal, heath, and grassland areas. The highest productivity was observed in Fennoscandian herb-rich forests (9050), followed by alluvial forests (91E0) (Figure 9). The lowest TPROD values were found in siliceous rocky slopes with chasmophytic vegetation (8220), followed by alkaline fens. Among open fell habitat types, TPROD shows a gradient corresponding to the fertility gradient (Figure 10). In fen habitats, TPROD decreases as moisture levels increase (Figure 11). The habitat-specific differences in productivity will be further compared to observations and modelled gross primary productivity in Task 4.1 of the project.

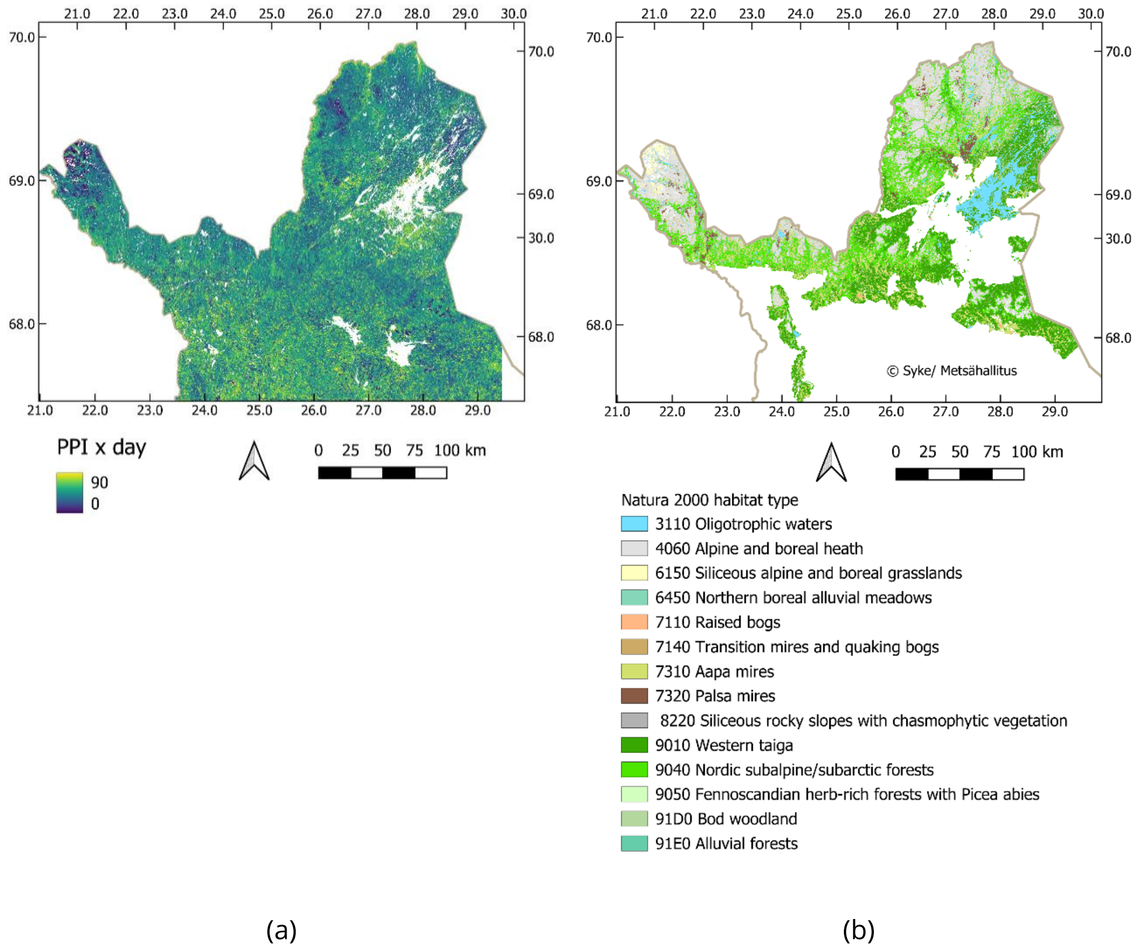

(a) (b)

Figure 9. Natura 2000 habitat types (a) and Copernicus HR-VPP total productivity, TPROD (Plant Phenological Index (PPI) x day) average for the period 2020-2023 in Northern Lapland (b).

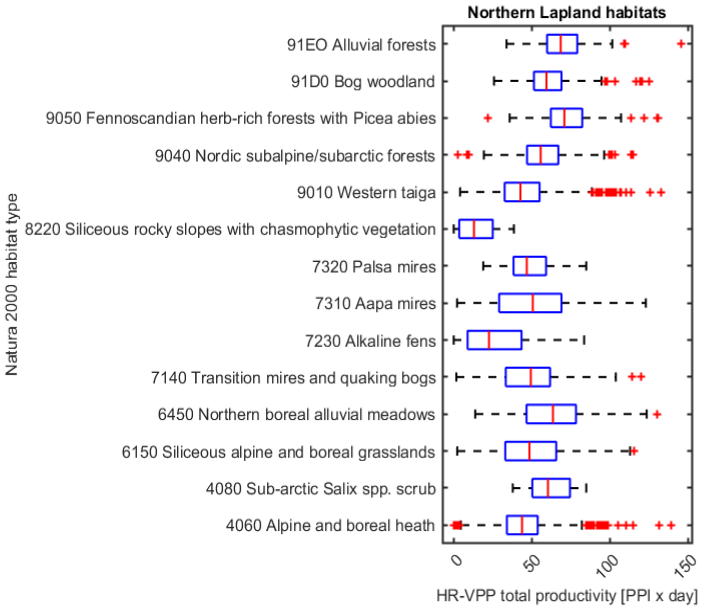

Figure 10. Boxplot visualising the summary statistics of the Copernicus HR-VPP total productivity (TPROD) metric (average for the period 2020-2023) by Natura 2000 habitat type in Northern Lapland. (The central red mark indicates the median, and the bottom and top edges of the box indicate the 25th and 75th percentiles, respectively. The whiskers extend to the most extreme data points not considered outliers, and the outliers are plotted individually using the red '+' marker symbol.)

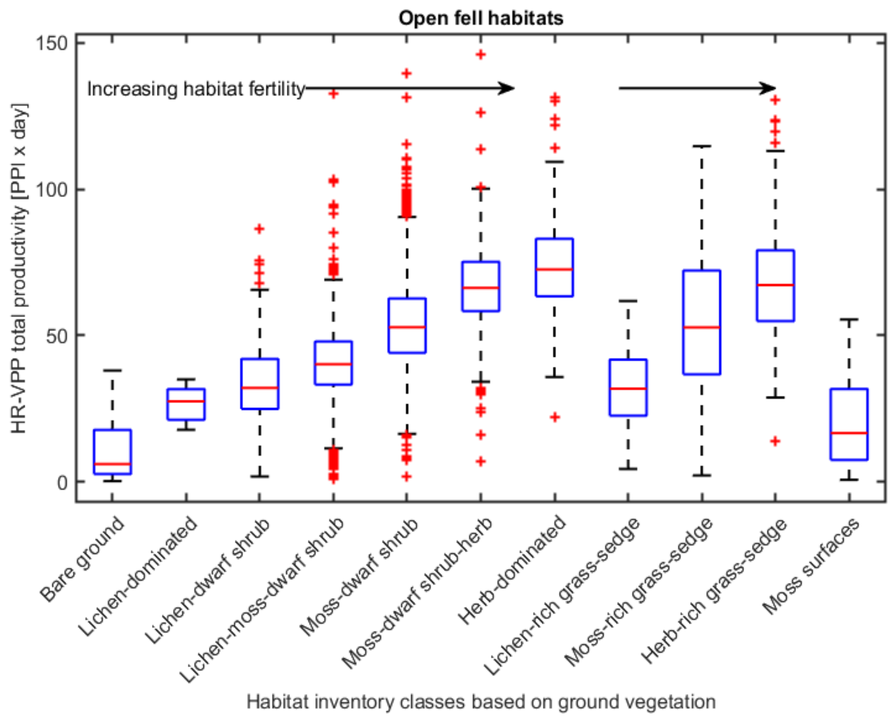

Figure 11. Boxplot visualising the summary statistics of the Copernicus HR-VPP total productivity (TPROD) metric (average for the period 2020-2023) by habitat inventory class for open fell areas in Northern Lapland.

The central red mark indicates the median, and the bottom and top edges of the box indicate the 25th and 75th percentiles, respectively. The whiskers extend to the most extreme data points not considered outliers, and the outliers are plotted individually using the red '+' marker symbol.

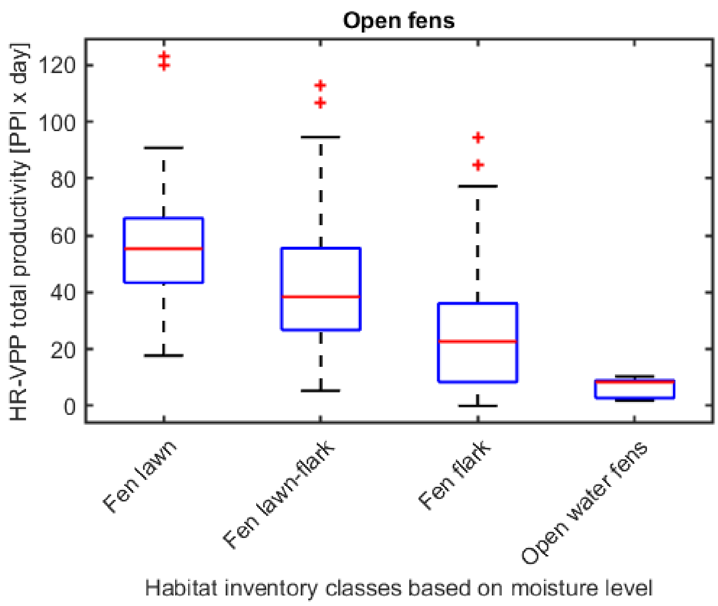

Figure 12. Boxplot visualizing the summary statistics of the Copernicus HR-VPP total productivity (TPROD) metric (average for the period 2020-2023) by habitat inventory class for open fens.

The central red mark indicates the median, and the bottom and top edges of the box indicate the 25th and 75th percentiles, respectively. The whiskers extend to the most extreme data points that are not considered outliers, and outliers are plotted individually using the red '+' marker.

3.7 Distribution of the Products

This case study used publicly available EO products rather than generating new EO datasets. Therefore, no project-specific EO products will be deposited or disseminated. The scientific findings and analyses derived from these products will be disseminated through peer-reviewed publications, project reports, and other BioClima dissemination channels.

4 Case study 3: Integrated EO and In-situ Assessment of Ecosystem Functioning Response to Climate Extremes in the Vysočina Region, Czech Republic

4.1 Introduction

The Czech BioClima case study demonstrates a reproducible workflow for relating ecosystem functioning to climate-related extreme events in a heterogeneous Central European rural landscape. The contribution combines satellite EO, UAV surveys, local microclimate and soil sensors, phytocoenological relevés, and laboratory soil analyses. For Task 2.1, the scope is deliberately narrowed to one candidate remotely sensed EBV (RS-EBV) in the ecosystem-functioning class—ecosystem phenology expressed through the magnitude and seasonal dynamics of vegetation activity—and one ECV—land surface temperature (LST). The remaining datasets are used for validation, environmental stratification, and interpretation; they are not presented as additional EBVs or ECVs.

4.2 Objective

The objective is to generate and document a coupled EBV-ECV product that characterises how vegetation activity changes before, during, and after heat, drought, frost, or disturbance episodes. The case study tests whether standardised Sentinel-2 vegetation activity metrics and Landsat LST can differentiate functional responses among young tree plantings, orchards, peatbog/wetland, spruce forests, and beech forest sites. Soil pH, mineral nitrogen, species composition, vegetation-layer cover, UAV observations, and local sensor series are explanatory and validation data. The present contribution does not claim identification of climate-resilient genotypes or causal management effects; these require longer time series and replicated experimental evidence.

4.3 Study area

The study area is located around Matějov in the Žďársko part of the Vysočina Region, Czech Republic. Three localities are divided into seven model sites representing young tree plantings, an orchard, a peat-bog habitat, a spruce forest, and a beech forest. The landscape is a temperate continental mosaic of agricultural land, forest stands, regeneration areas, grasslands, orchards, water-retention elements, wetlands, and linear landscape structures. This habitat diversity provides a suitable local test bed for comparing ecosystem functional responses under contrasting vegetation structure, stand age, soil acidity, nutrient status, and exposure to climate extremes.

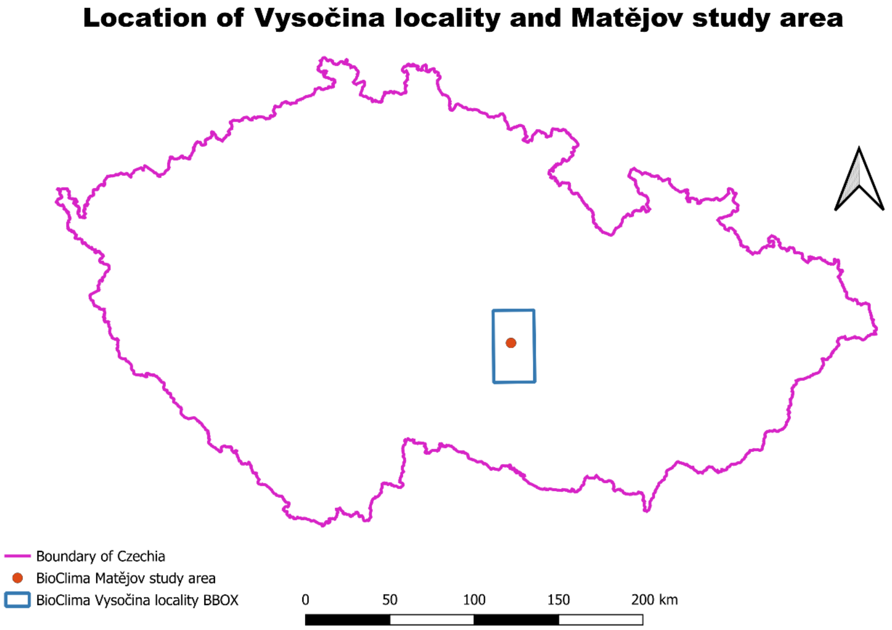

(a)

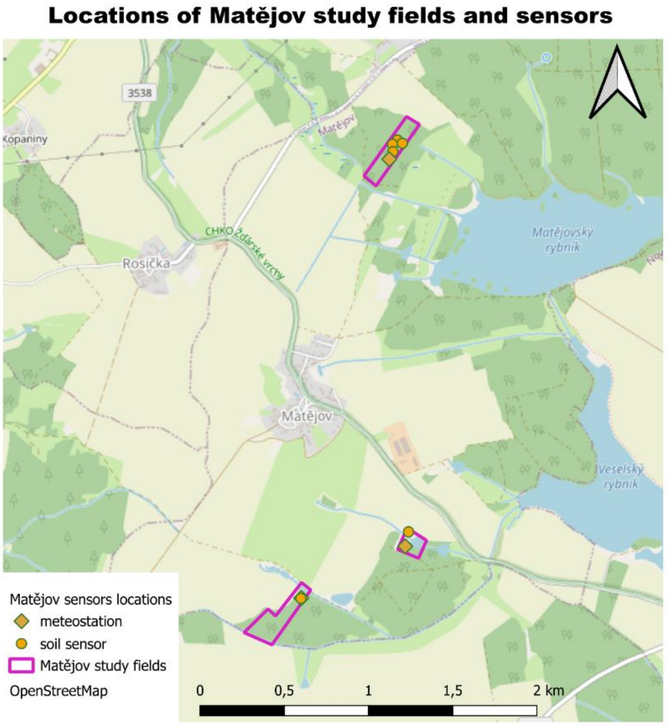

(b)

Figure 13. Location of Vysočina locality BBOX and Matějov study area (a) and the location of study fields in Matějov and in situ sensors

4.4 Vegetation-Composition and Soil Baseline

Phytocoenological relevés were collected at all seven sites using the Braun-Blanquet cover-abundance scale. The survey recorded tree-layer (E3), shrub-layer (E2), herb-layer (E1), and moss-layer (E0) cover, tree-layer age, slope, mineral nitrogen, and pH in upper and lower soil layers. These observations provide field-based information on species composition, successional stage, and habitat condition. They are used to stratify and interpret the EO-derived ecosystem-functioning response, rather than being treated as EO-derived EBVs.

Table 4. Summary of phytocoenological relevés and environmental characteristics at the seven study sites.

Site	Habitat	Vegetation layers (E3/E2/E1/E0)	Tree age/slope	Nmin upper/lower	pH upper/lower
1	Young tree planting	10 / 50 / 95 / 10	young / 5°	5.87 / 1.65	3.69 / 3.75
2	orchard	15 / 0 / 90 / 10	old / 5°	2.68 / 1.44	4.66 / 4.53
3	peat bog	0 / 35 / 70 / 30	young / 0°	2.68 / 1.32	3.46 / 3.74
4	spruce forest	30 / 0 / 30 / 60	old / 0°	2.83 / 0.84	3.17 / 3.81
5	beech forest	50 / 0 / 2 / 10	old / 0°	0.92 / 0.74	3.46 / 3.91
6	Young tree planting	0 / 50 / 80 / 10	young / 0°	0.68 / 1.69	3.83 / 3.06
7	Young tree planting	15 / 60 / 20 / 5	young / 0°	16.29 / 5.91	3.47 / 3.83

4.5 Data Sources

The assessment integrates: (i) Sentinel-2 multispectral observations from 2025 to the reporting date; (ii) Landsat thermal observations from 2025 to the reporting date; (iii) UAV true-color, multispectral, and elevation products acquired in spring 2026; (iv) ERA5-Land climate data for Czechia from 1950 to the present, used to provide the long-term climate context; (v) three Atmos41 weather stations, three VP-3 near-ground temperature and humidity sensors, and sixteen 5TM soil-water-content and soil-temperature sensors; (vi) phytocoenological relevés from seven sites; and (vii) fourteen laboratory soil samples collected on 29 April 2026 and analysed between 29 April and 21 May 2026 by the accredited Laboratory of Elemental Analysis at VŠÚO Holovousy.

- **Data Types and Their Role**

Sentinel-2 surface-reflectance bands support the vegetation-activity time series used to derive the candidate RS-EBV. Landsat Collection 2 Level-2 surface-temperature data support the selected ECV. UAV imagery provides sub-meter information for checking mixed pixels and local vegetation heterogeneity. ERA5-Land, weather-station, and soil-sensor records identify and contextualise heat, frost, and moisture-stress periods. Species composition, vegetation-layer cover, stand age, soil pH, mineral nitrogen, mineral elements, and heavy-metal measurements provide explanatory covariates for interpreting differences among sites. Soil pH and mineral nitrogen are environmental variables, not ECVs.

- **EO Datasets and Products**

The following EO inputs and derived products have been harvested or generated for the defined Vysočina locality:

- Copernicus Sentinel-2 multispectral scenes from 2025 to the reporting date; cloud-masked surface-reflectance bands are used where available.
- NASA/USGS Landsat thermal scenes from 2025 to the reporting date, used for the LST-ECV product.
- Derived visualisation and analysis products: NDVI, Enhanced Vegetation Index (EVI), Normalised Difference Red Edge Index (NDRE), Soil-Adjusted Vegetation Index (SAVI), Normalised Difference Water Index (NDWI), true-color imagery, and related quality layers.

Figures 14 and 15 document the successful generation of a Sentinel-2 true-color product and an NDVI vegetation-activity product for 29 May 2026.

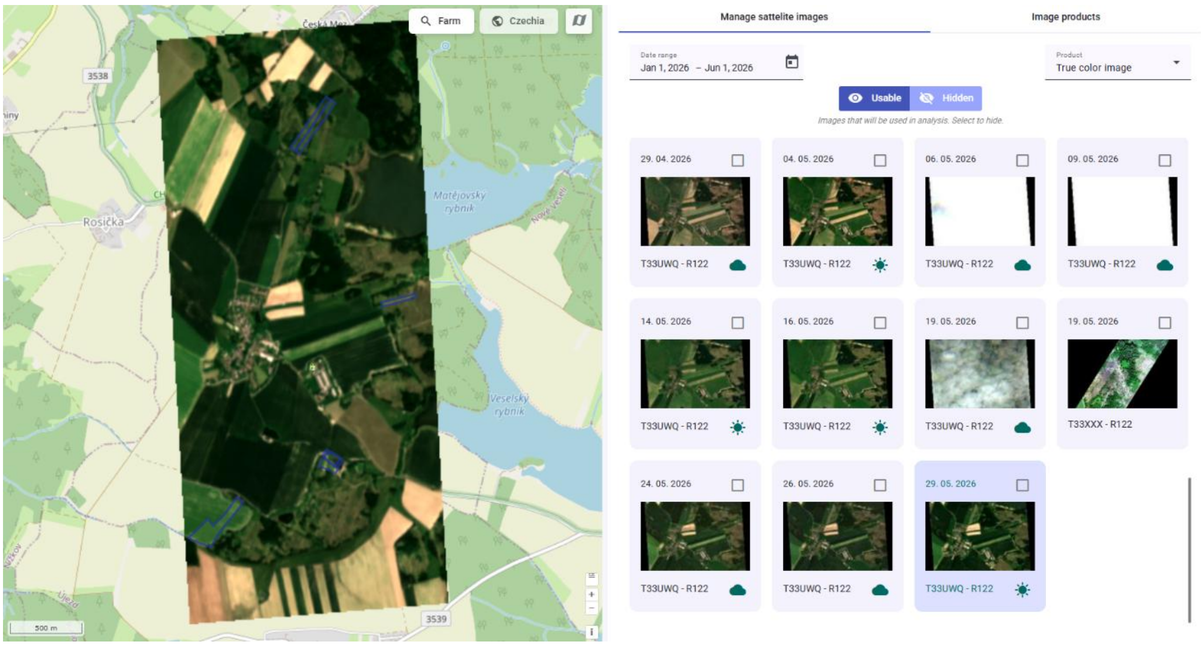

Figure 14. Sentinel-2 true-colour product for 29 May 2026.

Figure 15. Sentinel-2 NDVI vegetation-activity product for 29 May 2026.

- **Aerial Imagery**

The Matějov study fields are mapped twice per year using multispectral and photogrammetric UAV cameras. The first 2026 campaign used Wingtra-1 and produced:

- True colour orthophoto at 0.25 m pixel size;
- Multispectral imagery (blue, green, red, red-edge, and near-infrared) at 0.75 m pixel size;
- Digital elevation model at 1 m pixel size.

The UAV products are used to validate and interpret within-site heterogeneity and mixed Sentinel-2 or Landsat pixels (Figure 16).

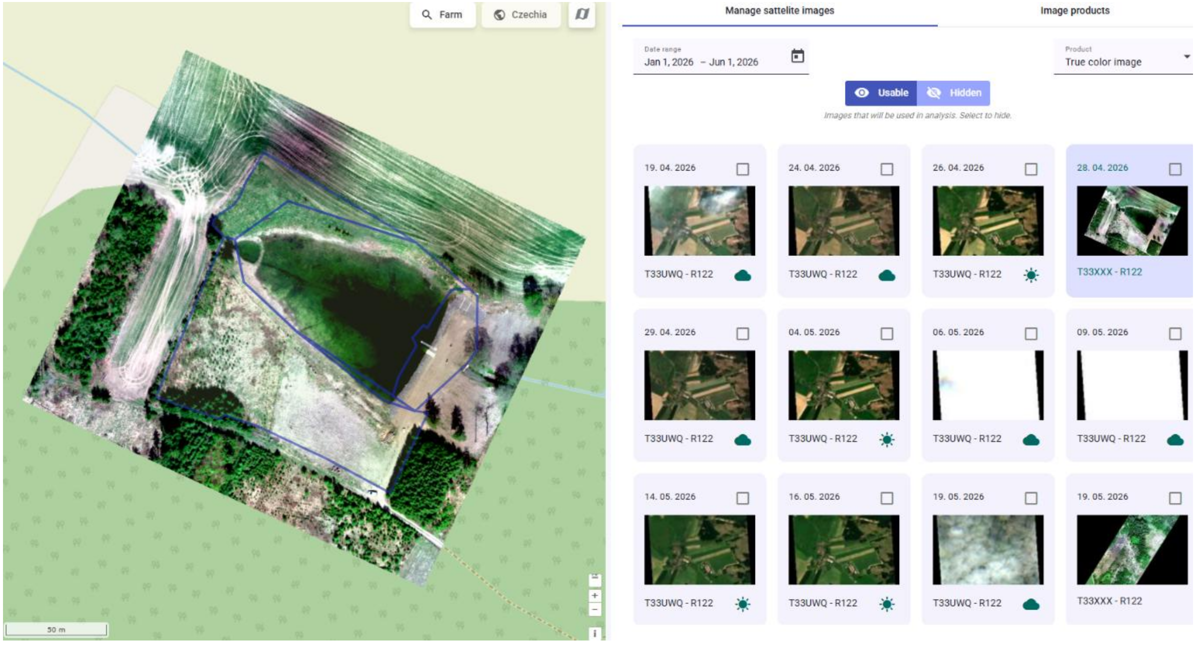

(a)

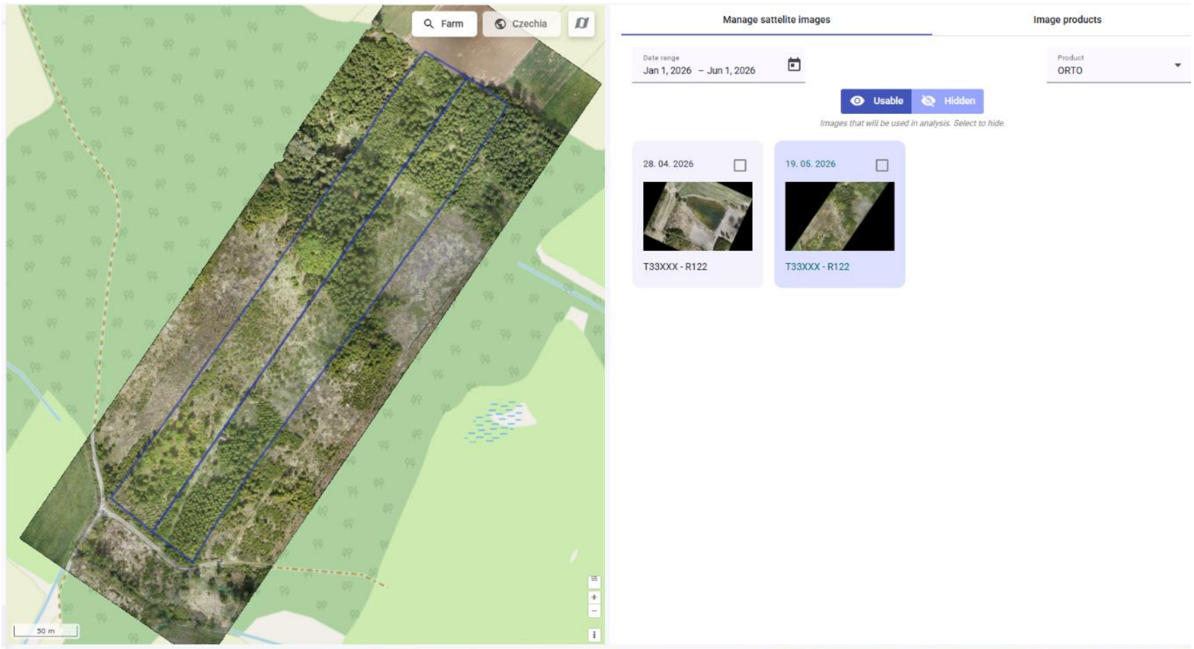

(b)

Figure 16. UAV multispectral image of a selected subarea, 28 April 2026 (a), and UAV true colour orthophoto of a selected subarea, 19 May 2026 (b).

- **Climate Context from ERA5-Land**

ERA5-Land data have been harvested for Czechia from 1950 to the present and used to calculate agroclimatic factors. For T2.1, these data provide the long-term reference for identifying anomalously warm, cold, or dry periods and for interpreting the shorter EO and local-sensor records. Examples of the available agroclimatic factors are shown in Figure 17.

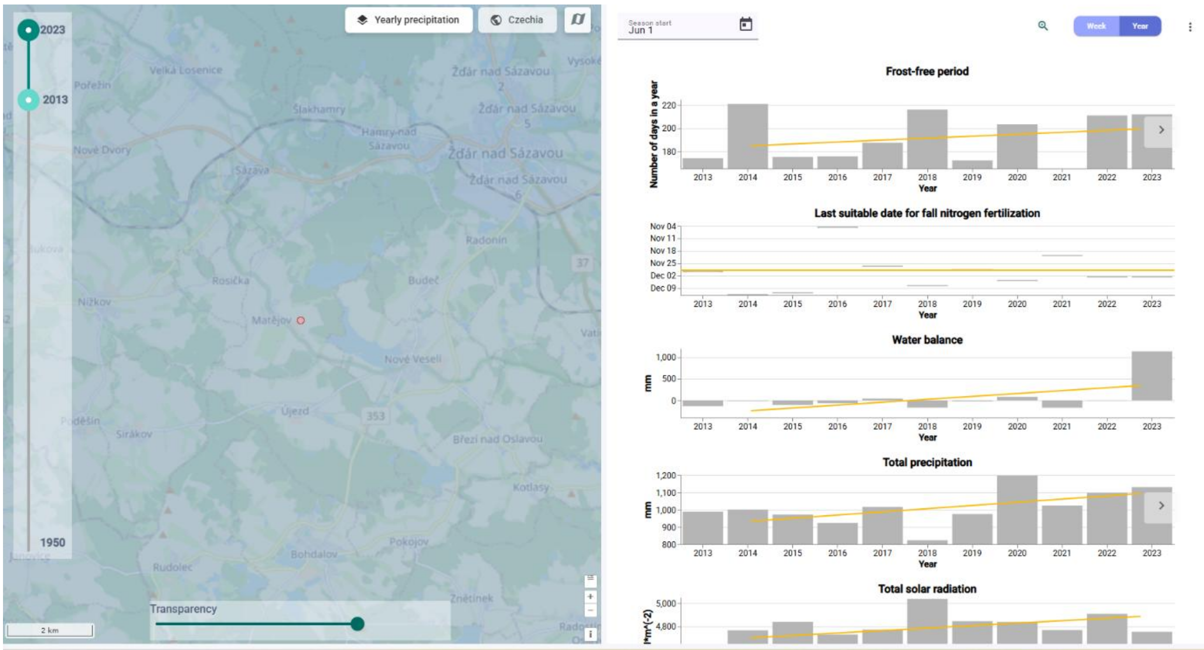

Figure 17. Example of agroclimatic factors calculated for 2013-2023.

- **Local Sensor Data**

Three subareas are equipped with weather stations and soil sensors. The deployed instruments are:

- Three Atmos41 all-in-one weather stations;
- Three VP-3 vapour-pressure, air-temperature, and relative-humidity sensors;
- 16 5TM volumetric water content and soil-temperature sensors.

Weather stations measure at 10-minute intervals and soil sensors at hourly intervals. VP-3 sensors represent near-ground atmospheric conditions at approximately 10 cm above the surface, while 5TM sensors are installed at approximately 10 and 30 cm depth (Figure 18). These observations validate timing and local contrasts but are not substitutes for the selected satellite LST-ECV, which represents radiometric surface skin temperature.

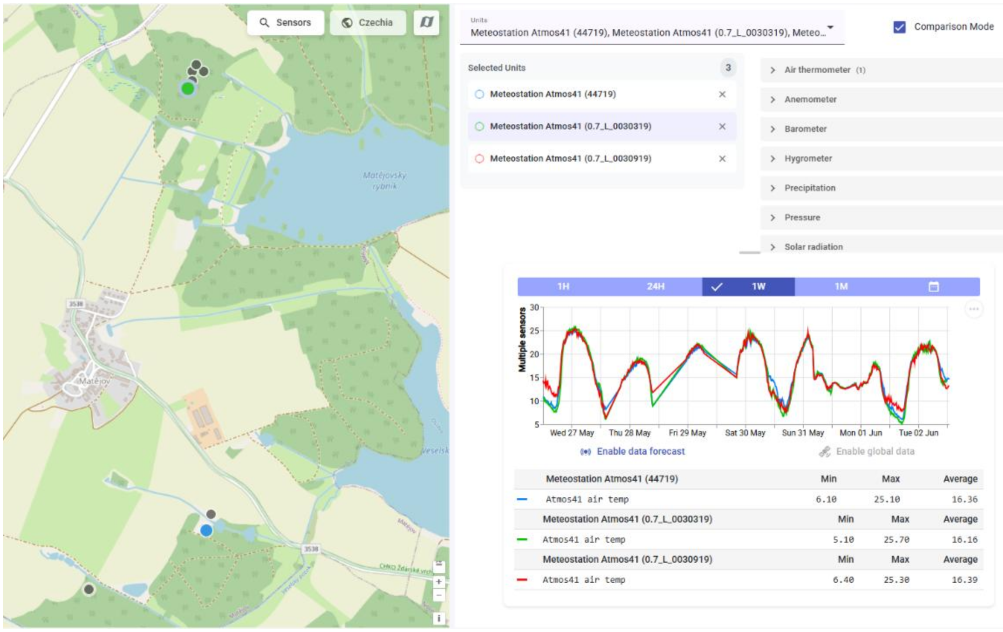

(a)

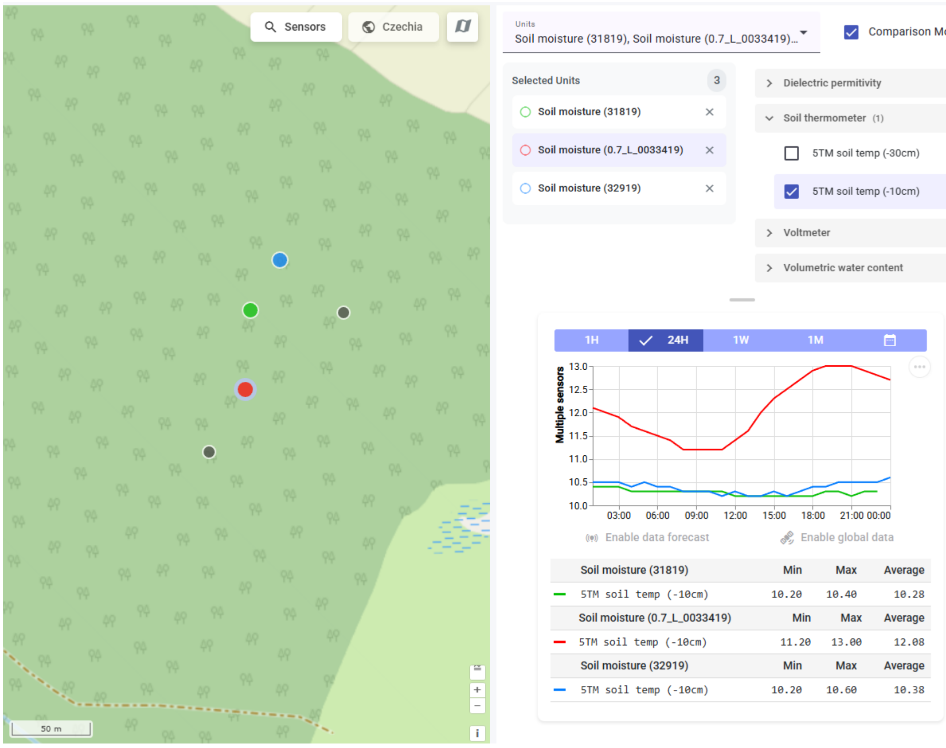

(b)

Figure 18. Example of air-temperature measurements from the three weather stations over seven days (a), as well as an example of soil-temperature measurements at 10 cm depth over 24 hours (b).

- **Selected RS-EBV and ECV**
    - **Candidate RS-EBV - ecosystem phenology (vegetation-activity magnitude and seasonal dynamics):**

Ecosystem phenology belongs to the ecosystem-functioning EBV class and describes the duration and magnitude of cyclic ecosystem processes, including vegetation activity. The operational EO measurement is a quality-controlled Sentinel-2 NDVI time series at 10 m spatial resolution. NDVI is not treated as the EBV itself; it is the remotely sensed measurement from which phenology metrics are derived. The metrics include the start and end of the season, the date and magnitude of peak activity, the seasonal amplitude, and the integral of vegetation activity. The currently documented product is the spatial magnitude of vegetation activity on 29 May 2026; the same workflow is applied to the complete time series.

- **Selected ECV - land surface temperature:**

LST describes the radiometric skin temperature of the land surface. It is derived from Landsat Collection 2 Level-2 surface-temperature data at 30 m spatial resolution. LST is selected because it directly characterises surface heating during extreme-temperature events and can be spatially coupled with the Sentinel-2 vegetation-activity product. It is not interchangeable with near-surface air temperature. Local Atmos41, VP-3, and 5TM observations are, therefore, used as contextual and validation data. The coupled T2.1 result is a site- and pixel-level comparison of vegetation-activity anomalies with contemporaneous LST anomalies.

This directly addresses ecosystem functioning responses to climate-related extreme events and avoids the broader, unsupported claim that the present dataset already identifies climate-resilient species or genotypes.

Table 5. Overview of the remote sensing variables, processing workflow, and outputs used in T2. 1.

Component	Selected variable	Primary input	Calculation	Reported output	Role in T2.1
RS-EBV candidate	Ecosystem phenology /vegetation activity	Sentinel-2 red B4 and NIR B8, 10 m	Cloud mask; NDVI; temporal compositing and smoothing; seasonal threshold metrics	NDVI raster; start/peak/end dates; amplitude; seasonal integral	Quantifies ecosystem-functioning state and change
ECV	Land surface temperature	Landsat Collection 2 Level-2 ST, 30 m	QA mask; scale factor and offset; conversion to degrees Celsius; site statistics	LST raster; median, P10, P90, maximum, anomaly	Represents surface thermal stress

Component	Selected variable	Primary input	Calculation	Reported output	Role in T2.1
Validation and interpretation	UAV, ERA5-Land, sensors, vegetation and soil data	UAV 0.25-0.75 m; climate and field observations	Spatial aggregation, temporal matching, stratification by habitat, stand age and soil condition	Quality flags, explanatory tables, uncertainty statement	Tests plausibility and limits attribution bias

4.6 Methodology

The following subsections present the methodologies applied in this case study.

4.6.1 Operational calculation and analysis workflow

- ***EO Data Pre-processing***

Sentinel-2 and Landsat scenes are spatially subset to the study area and linked to source-scene identifiers and acquisition metadata. Cloud, cloud-shadow, snow, saturation, and invalid pixels are excluded using the available quality layers. Products are retained at their native spatial resolution; resampling for visualisation does not increase analytical precision.

- ***Candidate RS-EBV Calculation***

For each valid Sentinel-2 observation, NDVI = (B8 - B4) / (B8 + B4), where B8 is near-infrared reflectance and B4 is red reflectance. Observations are composited to a regular temporal interval using the median of valid pixels and smoothed to reduce residual atmospheric and cloud contamination. For each pixel or site, the seasonal amplitude is A = NDVImax - NDVImin. A default relative threshold of NDVImin + 0.20A is used to determine the start of the season on the rising limb and the end of the season on the falling limb; the threshold is retained as a documented parameter and tested for sensitivity. Peak date and peak NDVI are extracted from the smoothed curve. The seasonal vegetation-activity integral is calculated as the time integral of NDVI above the seasonal minimum and reported in index-days.

- ***ECV Calculation***

For Landsat Collection 2 Level-2 surface-temperature pixels, temperature in Kelvin is calculated as LSTK = DN x 0.00341802 + 149.0 and converted to degrees Celsius as LSTC = LSTK - 273.15. For each site and acquisition, the median, 10th percentile, 90th percentile, and maximum valid LST are reported. The 30 m LST pixels are analysed separately from the 10 m Sentinel-2 pixels and are aggregated to common site polygons for comparison.

- ***Extreme-event and Response Assessment.***

ERA5-Land provides the long-term temporal context, while local sensors confirm event timing and near-ground conditions. For a defined event window, the vegetation response is calculated as the difference between the median NDVI or phenology metric during/after the event and the corresponding pre-event or seasonal reference. LST anomaly is calculated relative to the reference distribution for the same period. The EBV and ECV are joined by site, pixel support, and acquisition window. Results are stratified by habitat type, stand age, soil pH, and other available covariates. This procedure supports the identification of differential functional response; causal attribution requires repeated events and longer observation series.

4.7 Results

The following subsections present the results of this case study.

4.7.1 EO-derived RS-EBV Result

The processing chain has generated Sentinel-2 vegetation products for the Vysočina locality from 2025 onward, including the NDVI product shown for 29 May 2026. The product demonstrates that vegetation activity magnitude can be mapped consistently at 10 m resolution and that substantial spatial heterogeneity exists within and among forest, orchard, grassland, wetland, regeneration, and open/disturbed surfaces. The UAV multispectral data at 0.75 m and orthophoto at 0.25 m confirm fine-scale heterogeneity that may be mixed within a Sentinel-2 pixel. The current result should therefore be reported as a spatially explicit ecosystem phenology/vegetation activity product and an operational time-series method, rather than as a direct measurement of net primary productivity.

4.7.2 EO-derived ECV Result

Landsat thermal observations from 2025 onward have been harvested for the locality and serve as input to the LST product. The ECV is spatially compatible with site-level comparison and can be matched to Sentinel-2 observation windows. The source files supplied for this revision do not contain exported numerical LST summaries; consequently, no temperature range is invented in the narrative. The accompanying T2.1 product package should contain the scene-level LST rasters and the site-level median, P10, P90, maximum, and anomaly statistics generated by the documented workflow.

4.7.3 Field and Laboratory Interpretation

The vegetation survey identified three main species-composition groups: the orchard with Malus domestica and meadow species; a distinct beech-forest group dominated by Fagus sylvatica; and a larger group comprising young tree plantings, part of the peat bog site, and spruce-forest vegetation with a compositionally similar composition. DCA produced a gradient length of 5.82; the first two axes explained 36.82% and 14.56% of total variability. CCA identified tree-layer age and soil pH as the strongest examined controls on species composition. Tree-layer age explained 26.3% of variability ($F = 1.79$, $p = 0.012$), and upper-soil pH explained 33.78% ($F = 2.6$, $p = 0.044$). Tree-canopy cover, mineral nitrogen, and slope were not significant in the reported analysis.

4.7.4 Edaphic Context and Implication for EBV-ECV Interpretation

The fourteen soil samples show strongly acidic conditions, with pH ranging from 3.06 to 4.66, and marked variability in mineral nitrogen, ranging from approximately 0.68 to 16.29 mg/kg dry matter. Chromium exceeded the listed value of 100 mg/kg in both orchard/pond samples, and cadmium reached or exceeded the listed value in selected samples. These variables may influence vegetation activity independently of short-term thermal stress. Accordingly, the EBV-ECV response must be stratified by habitat and edaphic context and not interpreted as a climate effect without controlling for these factors.

The Vysočina contribution is therefore wrapped as one coupled product: (i) a candidate RS-EBV for ecosystem phenology/vegetation activity derived from Sentinel-2 and (ii) the LST ECV derived from Landsat. The scientifically supportable result is the demonstrated capacity to map ecosystem-functioning state, relate it to surface thermal conditions, and interpret differences using UAV, sensor, vegetation, and soil observations. The present evidence does not yet support claims regarding genotype adaptation, long-term ecosystem resilience, or causal management performance.

The workflow is transferable to comparable Central European agricultural-forest mosaics because it uses standard satellite products, explicit equations, parameterised thresholds, and polygon-based site aggregation. Transfer requires only a study-area geometry, habitat/site polygons, Sentinel-2 and Landsat observations, and optional local validation data. Site-specific parameters—cloud thresholds, phenology threshold, event windows, and baseline periods—are stored with product provenance and can be recalibrated. d. The same workflow can be extended to a longer Sentinel-2 archive and to additional sites without changing the EBV or ECV definition.

4.8 Distribution of the Products

The generated products will be distributed via the JackDaw Data Cube/Plan4all infrastructure and linked from the official BioClima project website. Public summaries and best-practice guidance will be published within one month of the contribution's completion. Access will follow the project's Data Management Plan, source data licenses, and restrictions applicable to precise fields or sensor locations. Each release will contain the following components:

Table 6. Summary of the T2.1 data products, formats, and access mechanisms.

Product	Format	Access Mechanism	Minimum Metadata/Quality Information
RS-EBV vegetation-activity and phenology rasters	Cloud Optimised GeoTIFF / GeoTIFF; browse tiles	JackDaw catalogue and map viewer; OGC API - Tiles/Coverages or equivalent project service	Input scene IDs, acquisition time, cloud mask, spatial resolution, CRS, processing version, threshold parameters
RS-EBV site time series and metrics	CSV or Parquet	Download the endpoint and the catalogue record	Site identifier, date, valid-pixel count, NDVI statistics, start/peak/end dates, amplitude, integral, uncertainty flags
LST-ECV rasters and site statistics	GeoTIFF/COG and CSV or Parquet	JackDaw catalogue and download endpoint	Landsat product ID, QA mask, scaling, units, valid-pixel count, median, P10, P90, maximum, anomaly
Coupled EBV-ECV event-response product	CSV/JSON and figures in the deliverable	Web application and downloadable package	Reference period, event window, spatial support, response metric, covariates, limitations
Validation and explanatory datasets	GeoPackage/CSV and PDF method note	Open where permitted; restricted/generalised where required	Sampling method, sensor calibration, laboratory method, uncertainty, licence, access condition

4.9 Data Access and Product Repositories

The Vysočina pilot products are now linked to two complementary repositories. The EO-derived products are exposed through the local cloud infrastructure via an OGC STAC endpoint, while in-situ sensor measurements used for event timing, validation, and interpretation are stored in SensLog and are currently accessible via REST/JSON endpoints. This distinction keeps the T2.1 deliverable focused on the EO-derived RS-EBV and ECV products, while presenting the sensor data as supporting validation and contextual information.

Table 7. Access routes for Vysočina / Matějov T2.1 data products.

Repository/ Service	Data Content	Role in T2.1	Access Endpoint/Mechanism
Local EO cloud / OGC STAC	Sentinel-2 vegetation-activity / phenology products and Landsat-derived LST products for the Vysočina / Matějov pilot.	Primary access route for the EO-derived T2.1 data products: RS-EBV candidate and ECV product package.	STAC API: https://aliance.hsrs.cz/eo-api/stac/ Matějov collection: https://aliance.hsrs.cz/eo/stac/collections/18_matejov
SensLog REST/JSON	Atmos41 weather stations, VP-3 near-ground air-temperature / humidity sensors, and 5TM soil-water-content / soil-temperature sensors.	Supporting in-situ data for event timing, local validation, interpretation of EO-derived anomalies, and uncertainty assessment. These data are not introduced as additional EBVs or ECVs.	GetUnits: https://senslog.lesprojekt.cz/senslogOTS4/rest/unit?user=Focal&type=full_units GetObservations templates are listed below.
Planned OGC SensorThings API	Standardised access to the same sensor measurements once the endpoint is deployed.	Improves interoperability of the in-situ validation stream. It should be referenced as planned, not as already operational.	Planned for July 2026, according to the data-infrastructure update.

SensLog observation endpoint templates

https://senslog.lesprojekt.cz/senslogOTS4/rest/observation?unit_id=<unitId>&from_time=<fromTime>&to_time=<toTime>&limit=<limit>

https://senslog.lesprojekt.cz/senslogOTS4/rest/observation?unit_id=<unitId>&sensor_id=<sensorId>&from_time=<fromTime>&to_time=<toTime>&limit=<limit>

https://senslog.lesprojekt.cz/senslogOTS4/rest/observation?group_name=<groupName>&sensor_id=<sensorId>&from_time=<fromTime>&to_time=<toTime>&limit=<limit>

https://senslog.lesprojekt.cz/senslogOTS4/rest/observation?group_name=<groupName>&from_time=<fromTime>&to_time=<toTime>&limit=<limit>

Example SensLog queries

https://senslog.lesprojekt.cz/senslogOTS4/rest/observation?unit_id=1305167562256957&from_time=2026-06-20&to_time=2026-06-22

https://senslog.lesprojekt.cz/senslogOTS4/rest/observation?unit_id=1305167562256957&sensor_id=340230002&from_time=2026-06-20&to_time=2026-06-22

https://senslog.lesprojekt.cz/senslogOTS4/rest/observation?group_name=matejov&from_time=2026-06-20&to_time=2026-06-22

4.10 Limitations and Required Interpretation

The EO record currently documented in the case file begins in 2025 and is too short for a robust long-term trend or local climatology. ERA5-Land is therefore used for the climate context, while an extension of the earlier Sentinel-2 and Landsat archives is recommended for subsequent analyses. The field baseline comprises seven sites and a single vegetation survey, limiting causal inference. Landsat LST measures surface skin temperature rather than air temperature and may contain mixed 30 m pixels. Phenology thresholds and event windows must be reported and sensitivity tested. The site-to-laboratory-sample crosswalk should be verified before the final public release because the vegetation-assessment table and laboratory labels use different ordering for some locality/site identifiers.

5 Case study 4: Ecosystem Functioning Responses to Climate Change Stressors in Agricultural Grasslands of Flanders, Belgium

5.1 Introduction

The work of T2.1 in WP2 supports the Belgian BioClima case study, which focuses on climate-smart and biodiversity-enhancing grassland management in agricultural landscapes in Flanders, Belgium. This work aims to improve the understanding of climate impacts, particularly droughts, heatwaves, and hydrological variability, on the functioning of intensively managed and semi-natural grasslands. The Belgian contribution aims to integrate ECVs and EBVs, which are derived from EO and ancillary geospatial data, to assess ecosystem dynamics and resilience. Emphasis is placed on vegetation phenology, productivity, carbon sequestration potential, and the impact of different management regimes, such as mowing and resowing, on ecosystem functioning. This work also supports adaptive land management strategies and contributes to harmonised monitoring approaches within the BioClima project.

5.2 Objectives

The objectives are to:

- Monitor the responses of ecosystem functioning to climate variability and extreme climate-related events in agricultural grasslands, using EO-derived EBVs and ECVs.
- Analyse vegetation dynamics and productivity dynamics under different grassland management regimes.
- Assess the relationships between climate stressors, hydrological dynamics, and ecosystem functioning.
- Support the development of AI-driven geospatial analysis frameworks for climate-smart and biodiversity-enhancing land management.
- Contribute to the spatial identification of biodiversity hotspots and ecosystem resilience patterns across Flanders.

5.3 Study Area

The study area covers the Flanders Region in northern Belgium, which is located within the Atlantic biogeographical region. This region is characterised by a temperate oceanic climate (according to the Köppen classification, Cfb), with mild winters, moderate summers, and relatively evenly distributed precipitation throughout the year. Grasslands in Flanders range from intensively managed agricultural pastures to species-rich, semi-natural grasslands found in Natura 2000 protected areas and regional nature reserves (Figure 19).

The region experiences significant anthropogenic pressure due to intensive agriculture, nitrogen deposition, and urban sprawl. Projections of climate change indicate rising temperatures, altered precipitation patterns and an increased frequency of droughts and extreme weather events. These factors influence grassland productivity, phenology and ecosystem resilience.

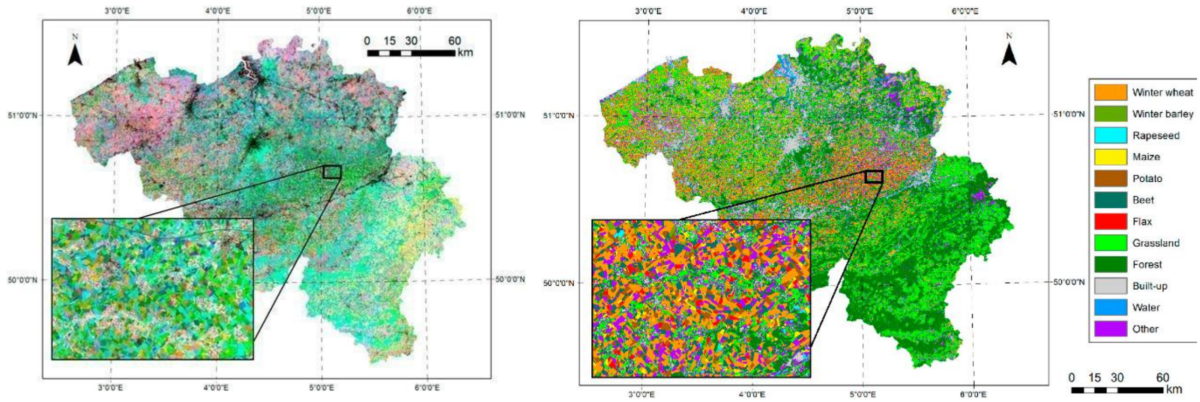

Figure 19. Sentinel-1/Sentinel-2-based Belgian maps illustrate agricultural landscape structure and land-cover heterogeneity relevant to the grassland case study (Van Tricht et al., 2018).

5.4 Data

- ***Data Sources Used***

The Belgian case study integrates multi-source EO, environmental, and in situ datasets, including Sentinel-1, Sentinel-2, and Sentinel-3 satellite observations; Copernicus Land Monitoring Service products such as HR-VPP and remote sensing-derived vegetation indicators (leaf area index, LAI; Fraction of Absorbed Photosynthetically Active Radiation (fAPAR); fractional vegetation cover (fCover); and NDVI); soil, hydrological, and topographic datasets; LPIS (Land Parcel Identification System) datasets; nature value geodata and biodiversity surveys; and climate datasets for temperature, precipitation, and drought analyses.

- **Data Types**

The analyses combine EO time series, in situ ecological and environmental observations, geospatial climate and hydrological datasets, land use and management information, and ancillary soil and terrain data.

- ***EBVs Applied***

The following EBVs related to ecosystem functioning are considered vegetation phenology indicators, such as growing length, ecosystem productivity, gross primary productivity, net primary productivity, LAI, fAPAR, fCover, NDVI, and species composition indicators at the parcel-to-landscape scale. At the landscape scale, land-cover and ecosystem-structure indicators are used (Figure 20).

- ***ECVs applied***

The following ECVs are integrated as climate stressor proxies: LST, soil moisture, evapotranspiration (ET), carbon-related variables and CO_2 fluxes, climate and hydrological anomaly indicators, and weather and drought time series indicators (such as SPEI).

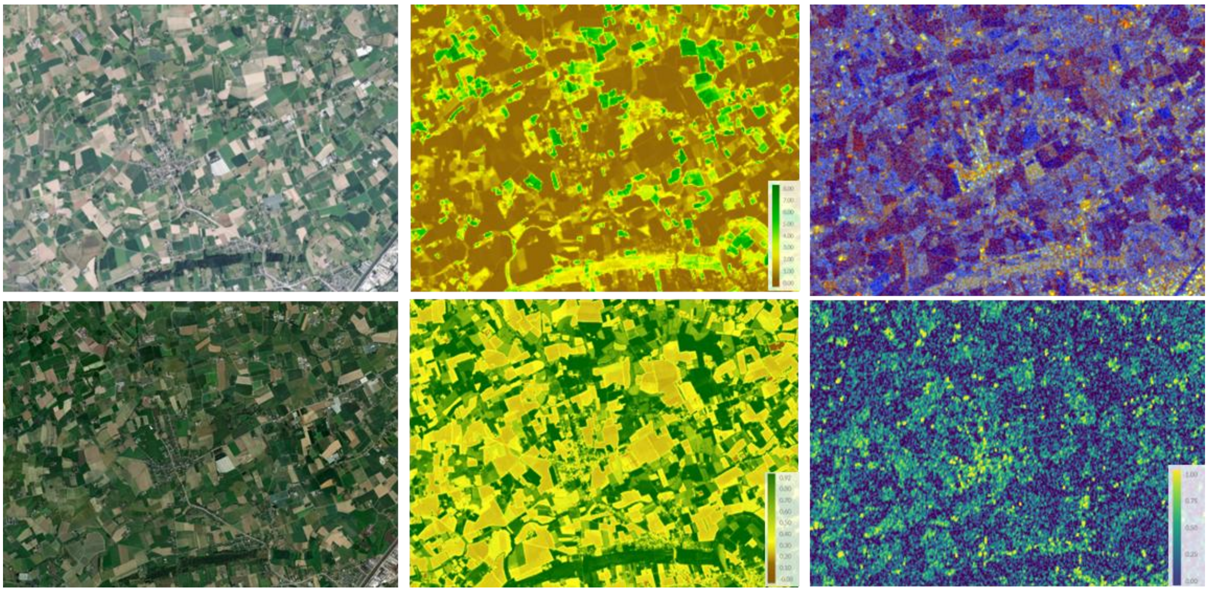

Figure 20. Data sources used from left to right: TOP - orthophotos, S2-LAI, S1-sigma0 and BOTTOM - Worldview, S2-NDVI, S1-coherence for location Deinze and surroundings in northern Belgium

5.5 Methodology

The contribution of the Belgian case study involves an integrated geospatial analysis that combines EO, environmental datasets, and artificial intelligence (AI)-driven modelling approaches.

Time series of EO data from Sentinel missions and Copernicus products are used to derive indicators of vegetation phenology and productivity associated with ecosystem functioning. Time-series analyses are then used to evaluate changes in vegetation activity and the resulting ecosystem response under varying climatic and management conditions. AI and machine learning approaches are currently explored to capture spatiotemporal dynamics in grassland systems and ecosystem functioning, including random forest regression. Spatial analyses integrate climate, hydrological, soil, and land-use information to identify biodiversity hotspots, assess ecosystem resilience and vulnerability, evaluate the impacts of droughts and extreme weather events, analyse ecosystem responses to mowing and resowing regimes, and assess the carbon sequestration potential. Model outputs will continue to be validated using field observations, remote sensing products, phenological indicators such as the length of the growing season, biodiversity monitoring datasets, and environmental statistics.

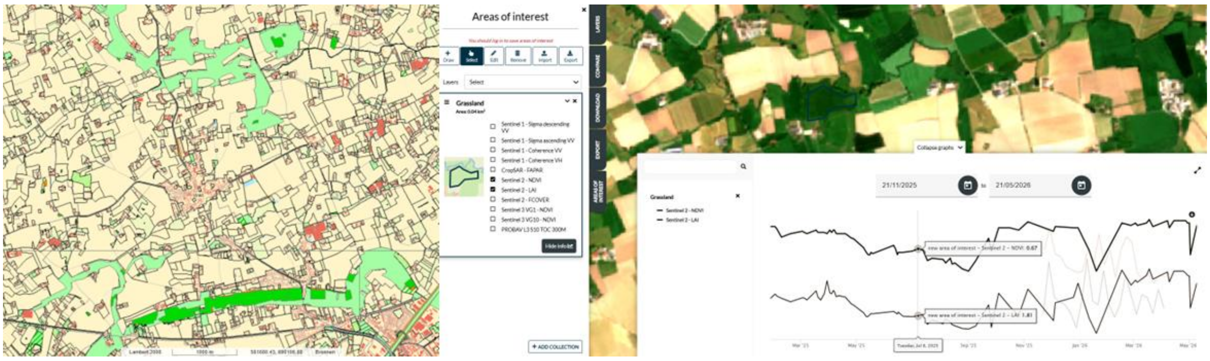

Figure 21. Biological value map (left) and time series NDVI and LAI reflecting hydrological dynamics.

5.6 Preliminary Results

The Belgian WP2.1 contribution is expected to generate spatially explicit indicators of grassland ecosystem functioning and resilience, EO-derived EBVs and ECVs for monitoring the impact of climate on managed grasslands in agricultural environments, detection of phenological shifts and productivity responses associated with climate variability and management intensity, identification of biodiversity hotspots and vulnerable grassland systems, improved understanding of the interactions between climate stressors, hydrology, land management, and ecosystem functioning; and develop AI-supported tools for adaptive and climate-smart grassland management.

These analyses will continue and are expected to support the regional implementation of targets from the EU Biodiversity Strategy, Natura 2000 management, the implementation of the Common Agricultural Policy (CAP), and climate adaptation planning.

The Belgian case study directly contributes to Task 2.1 by linking ecosystem functioning EBVs with climate-related ECVs, evaluating ecosystem responses to drought and heat stress, integrating multi-source EO products, contributing to harmonised methodologies for ecosystem monitoring, supporting AI-driven modelling frameworks developed in WP3, and providing spatially explicit ecosystem functioning indicators for climate adaptation and biodiversity assessment.

6 Case Study 5: Impacts of Climate Change-Related Extreme Events on the Ecosystem Functioning of the Mediterranean Pine Forest in Crete

6.1 Introduction

The Mediterranean Basin is warming substantially faster than the global average, with temperature increases estimated to be 20–40% higher than the global mean (Solano et al., 2025). Observed changes in temperature and precipitation patterns are expected to intensify under most future emission scenarios, increasing the frequency and severity of climate extremes across the region (Rakovec et al., 2022). Among these extremes, droughts and heatwaves are emerging as major drivers of ecosystem degradation (IPCC, 2023). Drought is commonly defined as a prolonged period of below-average water availability resulting from reduced precipitation and enhanced atmospheric water demand (Haied et al., 2023). It is one of the most economically and environmentally damaging natural hazards worldwide, although its impacts are often underestimated because of their gradual onset and diffuse nature (Wilhite et al., 2014). The 2018–2020 pan-European drought, one of the most severe on record, highlighted the vulnerability of Mediterranean ecosystems to prolonged and compound climate extremes. Importantly, drought impacts are amplified by rising temperatures. Increased evaporative demand accelerates soil moisture depletion and intensifies plant water stress, leading to reduced photosynthesis, elevated tree mortality, increased wildfire risk, and, in some cases, long-term ecosystem shifts (Clark et al., 2016; Yang et al., 2023). Given its hot, dry summers and drought-adapted vegetation, the Mediterranean region provides a natural laboratory for investigating interactions among drought stress, vegetation dynamics, and land surface temperature under climate change.

Drought affects ecosystem functioning across multiple biological scales. At the leaf level, water stress impairs photosynthetic processes, particularly Photosystem II, resulting in reduced light-use efficiency, photoinhibition, and oxidative damage (Lawlor & Cornic, 2002; Qiao et al., 2024). At the ecosystem scale, these physiological responses translate into substantial reductions in carbon uptake. Extreme drought events have been reported to decrease gross primary productivity by up to 50% and ecosystem respiration by approximately 32%, significantly altering ecosystem carbon balance (Ciais et al., 2005; Fu et al., 2020).

Mediterranean ecosystems are especially vulnerable because their functioning is strongly constrained by water availability. Open forests with sparse canopies have limited capacity to buffer temperature extremes and moisture loss (Italiano et al., 2023). Studies combining EO with dendrochronological analyses have revealed pronounced, species-specific declines in canopy condition and forest productivity during drought events (Italiano et al., 2023). Moreover, drought-induced reductions in vegetation cover can initiate positive feedback mechanisms: reduced transpiration lowers evaporative cooling, increasing LST, which further intensifies vegetation stress and canopy decline (Karinou et al., 2025). Heatwaves exacerbate these impacts through mechanisms that are partly independent of soil moisture deficits. Defined as periods of at least three consecutive days with exceptionally high temperatures, heatwaves have become more frequent, intense, and prolonged across the Mediterranean over recent decades (Perkins & Alexander, 2013). Consequently, heatwaves reduce carbon uptake, accelerate leaf senescence, and can cause irreversible tissue damage (Teskey et al., 2015). The combined occurrence of drought and heatwaves often generates impacts that exceed the effects of either stressor alone (Yin et al., 2023). Satellite-based studies in the western Mediterranean have shown that drought can reduce LAI by approximately 10% on average and by up to 23% in severely affected regions (Guion et al., 2022). Such declines can alter forest structure and ecosystem services for decades. Furthermore, drought legacy effects on soil microbial communities, nutrient cycling, and carbon dynamics can delay ecosystem recovery and increase vulnerability to subsequent disturbances (Van Der Molen et al., 2011).

By regulating the partitioning of incoming solar radiation into sensible and latent heat fluxes, LST influences evapotranspiration, soil moisture dynamics, and boundary-layer development, thereby affecting regional climate and the severity of climate extremes (Abdullah et al., 2025; Neinavaz et al., 2020). Because of its close relationship with vegetation water status and ecosystem functioning, LST is widely used to monitor drought stress, identify thermal anomalies, and assess vegetation responses to climate variability (Karinou et al., 2025; Li et al., 2023).

A robust and well-documented relationship exists between LST and vegetation characteristics such as NDVI and LAI. Dense and well-watered vegetation generally exhibits lower surface temperatures due to evapotranspirational cooling and canopy shading, whereas stressed vegetation often displays elevated LST, reflecting reduced water availability and diminished cooling capacity (Kliengchuay et al., 2025; Abdullah et al., 2025). In Mediterranean ecosystems, long-term remote sensing studies consistently report strong negative relationships between LST and vegetation greenness across seasonal and interannual timescales (Danopoulos et al., 2022). Furthermore, compound drought–heatwave events are frequently associated with elevated LST and substantial reductions in vegetation productivity and canopy condition (Karinou et al., 2025; Guion et al., 2022).

The interaction between LST and LAI represents a key vegetation–climate feedback mechanism, particularly in water-limited Mediterranean ecosystems. However, the spatial and temporal dynamics of this relationship remain insufficiently understood at scales relevant to forest management and conservation, especially in mountainous landscapes characterized by strong environmental heterogeneity (Stobbelaar et al., 2022; Abdullah et al., 2025). The LST–LAI relationship is governed by canopy energy balance processes. Drought-induced reductions in LAI decrease transpiration and canopy shading, resulting in higher surface temperatures. Elevated LST subsequently increases atmospheric water demand and promotes stomatal closure, reducing photosynthesis and accelerating leaf senescence. These processes create a positive feedback loop that can intensify vegetation stress and ecosystem degradation (Qiao et al., 2024; Kliengchuay et al., 2025).

Open coniferous forests dominated by Calabrian pine (*Pinus brutia*) provide an especially relevant system for investigating drought-driven LST–LAI interactions. Because canopy cover is naturally sparse, even moderate reductions in leaf area can result in substantial increases in surface temperature due to reduced shading and evaporative cooling (Eliades et al., 2018; Russo et al., 2019). These characteristics make Mediterranean pine forests highly sensitive to drought-induced thermal feedback. Nevertheless, relatively few studies have examined these dynamics in protected mountain landscapes of the eastern Mediterranean (Sebastiani et al., 2023; Italiano et al., 2023).

6.2 Objectives

This case study aims to improve understanding of vegetation responses to drought-driven climate extremes in Mediterranean open forests by integrating satellite-derived ECVs and EBVs. Specifically, it examines the spatiotemporal dynamics of LST and their relationship with changes in LAI under increasing drought stress.

The study has two main objectives as follows:

- Investigate LST variability over the past two decades and identify persistent LST hotspots.
- Assess the effects of LST dynamics on LAI.

6.3 Study Area

The study was conducted in the Samaria National Park, located in southwestern Crete, Greece. Crete, the largest island in Greece, lies in the eastern Mediterranean and is characterised by complex topography, diverse habitats, and a Mediterranean climate with hot, dry summers and mild, wet winters (Vogiatzakis et al., 2006; Kougioumoutzis et al., 2020) (Figure 22). Annual precipitation varies considerably, ranging from approximately 400 mm in coastal areas to over 2,100 mm in mountainous regions (Argyriou et al., 2016). Samaria National Park covers approximately 48.5 km² and extends from mountainous terrain through deep gorges and valleys to the Libyan Sea (Boteva et al., 2004; Manoutsoglou et al., 2022). The park supports diverse Mediterranean forests dominated by Mediterranean cypress (*Cupressus sempervirens*), Calabrian pine (*Pinus brutia*), and Cretan maple (*Acer sempervirens*), as well as numerous endemic plant species (Georghiou & Delipetrou, 2010; Bonari et al., 2021). Located in a semi-arid to dry sub-humid climatic zone, Crete is highly vulnerable to drought and desertification, with substantial areas classified as sensitive to land degradation (Kosmas et al., 1999; Morianou et al., 2018). In Samaria National Park, climate-related pressures, including drought, extreme weather events, and fire, increasingly threaten ecosystem functioning and biodiversity (Sabater et al., 2023). Consequently, understanding climate impacts on forest dynamics is essential for supporting conservation and adaptive management in Mediterranean ecosystems.

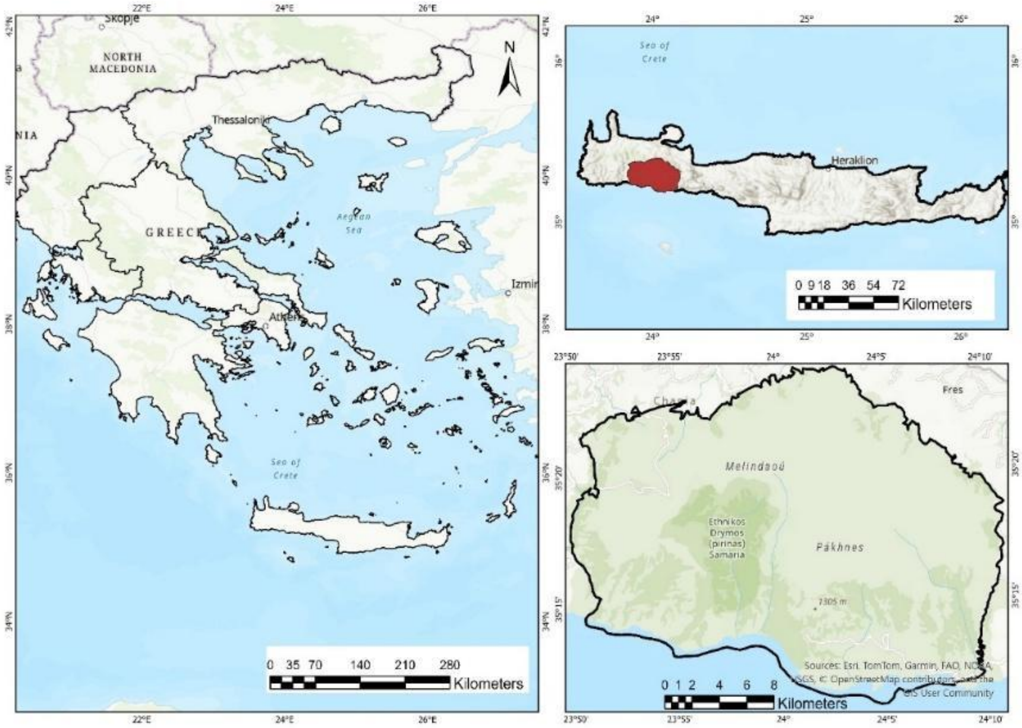

Figure 22. Samaria (Lefka Ori) National Park Study Area, located on the Island of Crete, Greece.

6.4 Data

- ***Data Sources Used***

This study integrates in situ LAI data, Sentinel-2 multispectral imagery, Landsat thermal infrared data, CORINE Land Cover data, and ERA5-Land climate reanalysis to investigate vegetation dynamics and drought impacts in Samaria National Park.

- ***Data Type(s)***

The CORINE Land Cover 2018 dataset (EEA, 2018) was used to generate a vegetation mask for the LST and LAI analyses. The original 100 m land-cover product was resampled to the 30 m Landsat grid using nearest-neighbour interpolation. Analysis was restricted to coniferous forest (Class 312), natural grassland (Class 321), and transitional woodland-shrub (Class 324) classes. This masking procedure excluded non-vegetated and built-up areas, reducing potential bias in hotspot detection and vegetation analyses. Climate data were obtained from the ERA5-Land reanalysis dataset produced by the European Centre for Medium-Range Weather Forecasts (ECMWF) under the Copernicus Climate Change Service (Muñoz-Sabater et al., 2021). ERA5-Land provides globally consistent land-surface climate variables at approximately 9 km of spatial resolution. Monthly precipitation and 2 m air temperature data for the period 2005–2025 were downloaded from the Copernicus Climate Data Store (Muñoz-Sabater, 2019). These variables were used to characterise climatic conditions across the study period and to derive the SPEI for drought assessment. ERA5-Land data indicate that Samaria National Park has a typical Mediterranean climate, with mean annual precipitation of 748 mm and mean annual potential evapotranspiration (PET) of 756 mm during 2005–2025. The close balance between water supply and atmospheric demand places the park near the transition between water-surplus and water-deficit conditions. Precipitation is concentrated in winter, while PET peaks during the dry summer months. Combined with the limited water-storage capacity of the karstic substrate, this strong seasonality makes vegetation highly dependent on winter rainfall. Consequently, variations in winter precipitation strongly influence summer water stress and the condition of Calabrian pine forests.

In-situ LAI data were collected during a field campaign conducted between November and December 2025. A total of 29 plots (30 × 30 m) were established to match the spatial resolution of Landsat and Sentinel-2 imagery. The plot size was selected to adequately represent the relatively homogeneous Calabrian pine stands that dominate Samaria National Park while minimizing mixed-pixel effects. Of the 29 surveyed plots, 28 provided complete datasets and were used for validation. LAI was estimated from hemispherical (fisheye) photographs acquired with a Canon EOS-6D camera equipped with a 15 mm fisheye lens, mounted 1.2 m above the ground. Five photographs were taken at each plot (one central and four cardinal positions) to capture canopy variability. Images were processed in Gap Light Analyser (GLA) v2.0, in which canopy and sky pixels were separated by thresholding the blue channel, which provides optimal canopy–sky contrast (Jonckheere et al., 2005; Macfarlane et al., 2007).

- ***EBVs Applied***

LAI was estimated using Sentinel-2 MultiSpectral Instrument imagery, which provides high spatial resolution (10–60 m) and frequent revisit times, making it suitable for vegetation monitoring. LAI retrieval was based on spectral information that is sensitive to canopy structure and vegetation condition (Clevers et al., 2017). LAI was estimated using a site-specific EVI approach (Huete et al., 2002) applying Sentinel-2 data. Four accuracy metrics were used to evaluate satellite-derived LAI against in-situ measurements: the coefficient of determination (R^2), RMSE ($m^2\ m^{-2}$), mean bias ($m^2\ m^{-2}$), and relative RMSE (rRMSE; %). Negative R^2 values were interpreted as indicating model performance worse than that of the sample mean as a predictor (Kvålseth, 1985; Chicco et al., 2021). The retrieval method with the highest R^2 and lowest RMSE was selected for subsequent analyses.

- ***ECVs Applied***

LST was derived from Landsat thermal infrared imagery, providing a continuous record from 2005 to 2025. For the period 2005–2012, thermal data from Landsat 5 TM and Landsat 7 ETM+ were used. From 2013 onwards, LST was retrieved from the thermal infrared sensor onboard Landsat 8 and 9. Only Band 10 (10.60–11.19 μm) was used because of its superior radiometric performance and lower susceptibility to stray-light contamination compared with Band 11 (Rozenstein et al., 2014). All thermal data were processed at a 30 m spatial resolution to enable long-term analysis of surface temperature dynamics using the Single-Channel (SC) algorithm of Jiménez-Muñoz and Sobrino (2003), which estimates surface temperature from a single thermal band and incorporates atmospheric and surface emissivity parameters (Sobrino et al., 2004).

6.5 Methodology

The following subsections present the methodologies applied in this case study.

6.5.1 Land Surface Temperature Hotspot Analysis

A hotspot analysis was conducted to identify areas of persistent thermal stress within Samaria National Park using summer (June–August) LST data from 2005 to 2025. A 21-year mean summer LST was calculated for each pixel to capture long-term thermal conditions while reducing the influence of interannual variability (Bento et al., 2020; Gu et al., 2016). To improve the robustness of hotspot detection, the 30 m LST data were aggregated to a 500 m × 500 m fishnet in ArcGIS Pro. This scale reduces pixel-level noise and atmospheric artifacts while preserving ecologically meaningful spatial patterns associated with topography and vegetation structure. The selected resolution also corresponds to the typical scale of mesoscale thermal variability in Mediterranean mountain environments. The Getis-Ord Gi* statistic (Getis & Ord, 1992; Ord & Getis, 1995) was applied to the aggregated LST data to identify statistically significant clusters of high and low temperatures. Spatial relationships were defined using a fixed-distance neighbourhood, and False Discovery Rate (FDR) correction was applied to account for multiple testing. Cells with Gi* z-scores ≥ 1.96 (95% confidence level) were classified as significant LST hotspots, representing areas of persistent thermal stress.

6.5.2 Standardized Precipitation Evapotranspiration Index

Meteorological drought was characterized using the SPEI, which quantifies climatic water balance by incorporating both precipitation and atmospheric evaporative demand (Vicente-Serrano et al., 2010). Unlike precipitation-based drought indices, SPEI is particularly suitable for Mediterranean environments because it captures the combined effects of reduced rainfall and elevated temperatures (Beguería et al., 2014). Rather than using the global SPEI dataset, which is too coarse to represent the complex topography of Samaria National Park, SPEI was calculated locally from ERA5-Land monthly precipitation and 2 m air temperature data for the period 2005–2025 (Muñoz-Sabater et al., 2021). PET was estimated using the Thornthwaite method (Thornthwaite, 1948), and the monthly climatic water balance was derived from the difference between precipitation and PET. The water-balance series was accumulated over 1-, 3-, 6-, and 12-month periods (SPEI-1, SPEI-3, SPEI-6, and SPEI-12) and standardized using a non-parametric approach based on the Gringorten (Gringorten, 1963) plotting position and inverse normal transformation. This method was selected because it provides more robust results for relatively short time series (Hao & AghaKouchak, 2014; Stagge et al., 2015). The four accumulation periods represent different drought-response timescales, ranging from short-term moisture deficits (SPEI-1) to longer-term hydrological conditions (SPEI-12). Drought severity was classified following McKee et al. (1993), with SPEI values below −1.0, −1.5, and −2.0 indicating moderate, severe, and extreme drought, respectively. For subsequent analyses, summer mean SPEI values (JJA; June, July, and August) were extracted for each year from 2005 to 2025. Years were classified as drought years when JJA mean SPEI fell below −1.0 at either the 6- or 12-month timescale, reflecting conditions most relevant to forest canopy water stress.

6.5.3 Annual Trend and Breakpoint Detection Using LandTrendr

Temporal changes in annual LST and LAI were analysed using the LandTrendr algorithm (Kennedy et al., 2010), implemented in Google Earth Engine (Kennedy et al., 2018). LandTrendr fits piecewise linear models to annual time series, enabling the identification of long-term trends, breakpoints, and the timing and magnitude of significant changes. Although originally developed for forest disturbance and recovery monitoring, the algorithm has since been widely applied to other environmental variables. The analysis was performed on annual summer (JJA) LST and LAI time series from 2005 to 2025. Because LandTrendr is designed to detect decreases associated with disturbance, the LST series was multiplied by −1 before segmentation, so that warming events were treated as disturbances. Following the analysis, all fitted values and change metrics were converted back to their original units (°C) by reversing the transformation. This approach enabled consistent detection of temporal trends and abrupt changes in both LST and LAI across the study area.

6.5.4 Joint Interpretation of Trends and Drought Events

To evaluate the influence of drought on thermal dynamics, annual summer (JJA) LST trajectories were compared with SPEI time series at four accumulation scales (SPEI-1, SPEI-3, SPEI-6, and SPEI-12). The SPEI scale that showed the strongest correspondence with LST variability was identified through visual comparison and subsequently used to assess whether LandTrendr-detected LST breakpoints coincided with drought years (SPEI <- 1.0). An integrated visualization combining LST anomalies, LAI anomalies, SPEI series, drought years, and LST breakpoints was produced to assess the temporal relationships among drought, warming, and vegetation responses.

6.5.5 Quantifying the Land Surface Temperature–Leaf Area Index Relationship

The relationship between LST and LAI was examined using plot-level analyses. Only plots with sufficient temporal coverage (≥8 LAI observations and ≥15 LST observations) were included in statistical testing. To remove the influence of persistent site characteristics such as elevation, aspect, and canopy density, analyses were performed using plot-specific anomalies calculated relative to a leave-one-out climatology.

Temporal trends in annual JJA-LST and LAI were assessed using the Mann–Kendall test and Theil–Sen slope estimator (Theil, 1950), following lag-1 autocorrelation correction through Yue–Pilon (Yue et al., 2002) pre-whitening. Trend magnitudes were reported in $°C\ yr^{-1}$ for LST and $m^2\ m^{-2}\ yr^{-1}$ for LAI.

The thermal environment was represented by two continuous descriptors: mean JJA-LST and long-term LST trend. Relationships between these variables and LAI metrics (mean LAI, LAI trend, and variability) were evaluated using ordinary least squares regression and Spearman correlation. Linear mixed-effects models were further used to test whether LAI trends varied along the thermal gradient.

The relationship between LST and LAI was investigated at annual, seasonal, and multi-year timescales. Annual analyses examined correlations between JJA-LST and concurrent or lagged LAI (0–3 years), while seasonal analyses assessed monthly relationships within the summer period. Multi-year analyses assessed whether cumulative heat exposure over the preceding 1–4 years better explained LAI variability than cumulative heat exposure over individual years.

All analyses were performed in Python using SciPy, statsmodels, and pymannkendall. Multiple testing was controlled using the Benjamini–Hochberg false discovery rate procedure (Benjamini & Hochberg, 1995), and results are reported using effect sizes and confidence intervals in addition to p-values.

6.6 Results

The following subsections present the results of this case study.

6.6.1 Land Surface Temperature Computation

LST was computed across Samaria National Park for the period 2005–2025. For illustration, Figure 23 presents the LST maps for three of the warmest summers in the study period: 2010, 2021, and 2024. In all three years, the highest temperatures (approximately 40–48 °C) were concentrated in the lower southern and south-eastern parts of the park, while the higher-elevation central areas remained substantially cooler (approximately 28–36 °C). The spatial extent of high-temperature areas was greatest in 2010, which also recorded the highest park-wide mean summer (JJA) LST (37.3 °C), compared with 37.1 °C in 2024 and 36.8 °C in 2021.

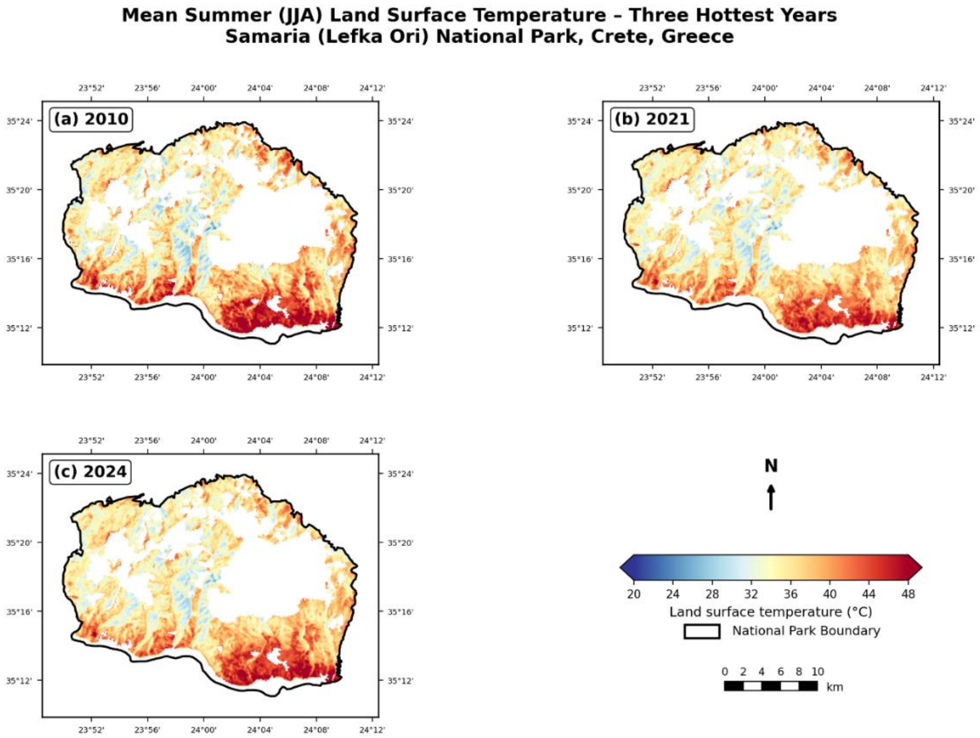

Figure 23. Spatial distribution of mean summer (June–August; JJA) Land Surface Temperature (LST) across the study area during the three warmest summers recorded between 2005 and 2025.

6.6.2 Land Surface Temperature Hotspot Analysis

The Getis-Ord Gi* hotspot analysis of the 21-year mean summer (JJA) LST revealed a clear north–south thermal gradient across Samaria National Park (Figure 23). Persistent Coldspots were concentrated in the northern and north-central interior of the park, whereas persistent Hotspots formed a continuous belt along the southern margin, indicating areas of recurrent thermal stress. This pattern closely reflects the park's topography, with cooler conditions occurring at higher elevations and warmer conditions at lower elevations. The transitional “Mostly Hot” and “Mostly Cold” classes occupied only limited areas surrounding the persistent hotspot and Coldspot cores. Much of Central Park was classified as non-persistent due to the vegetation mask. Importantly, all field sampling plots were located within the persistent Hotspot zone. Consequently, the plot-level analyses focus on the warmest and most thermally stable areas of the park, rather than on transitional or Coldspot environments.

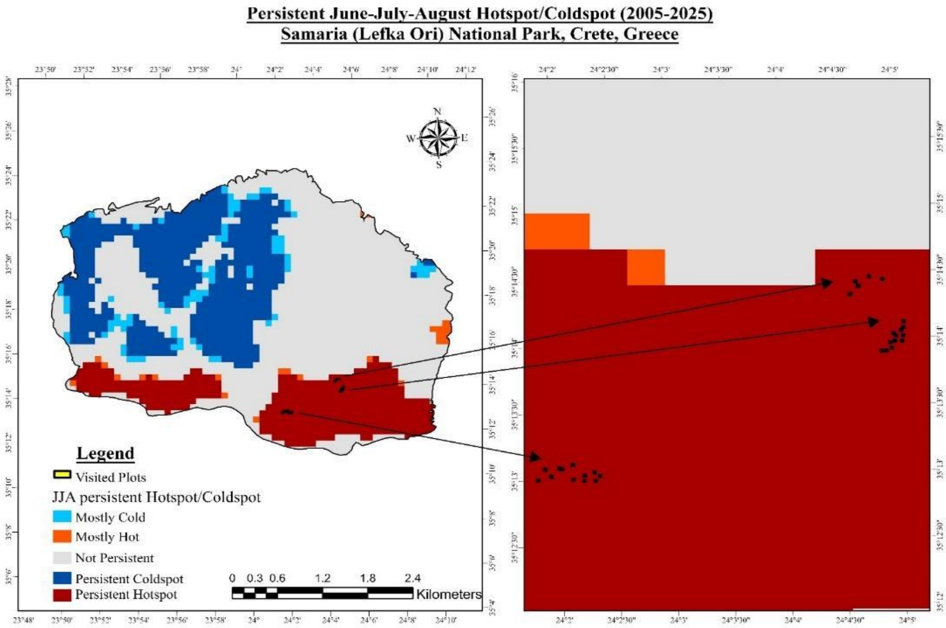

Figure 24. Persistent summer (JJA) LST Hotspots and Coldspots in Samaria National Park.

6.6.3 Land Surface Temperature Variation Across the Study Area

The mean summer (JJA) LST across Samaria National Park during 2005–2025 was 34.99°C. Summer temperatures varied from 32.25 °C in 2012, the coolest year on record, to 37.31 °C in 2010, the warmest year (Figure 24). The three warmest summers occurred in 2010 (37.31 °C), 2024 (37.07 °C), and 2021 (36.83 °C), whereas the coolest were recorded in 2012 (32.25 °C), 2017 (33.49 °C), and 2009 (33.71 °C). On a monthly scale, July was the warmest month (35.84 °C), followed by August (35.25 °C) and June (34.07 °C), reflecting the seasonal progression of summer heating in the Mediterranean region. A positive warming trend was detected over the study period, with a Theil–Sen slope of +0.070 °C yr^{-1}. However, the Mann–Kendall test indicated that this trend was not statistically significant ($\tau = 0.21$, $p = 0.194$), suggesting that interannual variability dominated the temperature record. Consequently, although summer LST increased over time, the warming signal was insufficiently strong to establish a significant long-term trend at the park scale.

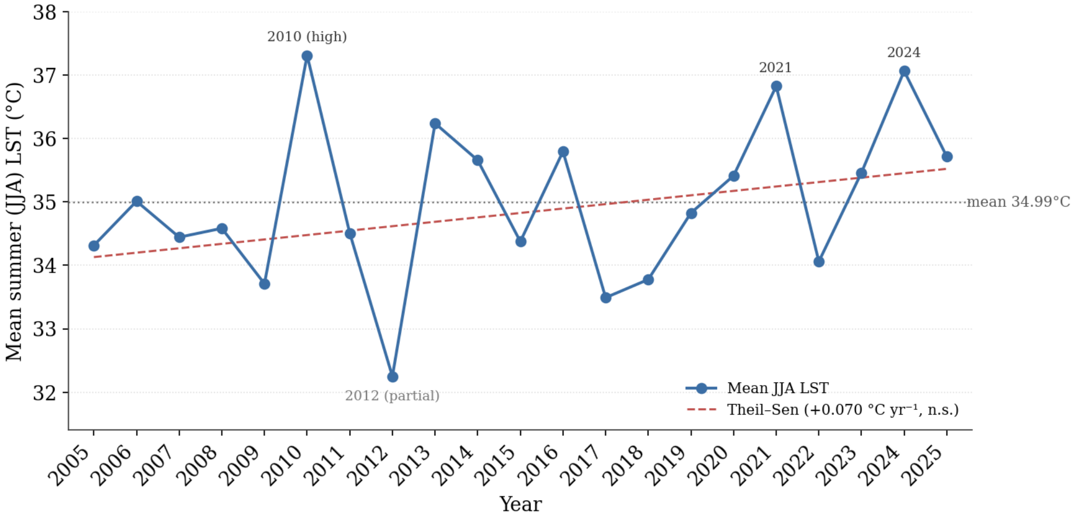

Figure 25. Annual park-wide mean summer (June–August; JJA) Land Surface Temperature (LST) for the period Drought Characterisation Using the Standardized Precipitation Evapotranspiration Index

Meteorological drought during 2005–2025 was characterized using the Standardized Precipitation Evapotranspiration Index (SPEI) calculated at four accumulation periods: 1, 3, 6, and 12 months (SPEI-1, SPEI-3, SPEI-6, and SPEI-12). Shorter accumulation periods reflect immediate moisture deficits, whereas longer periods capture seasonal-to-annual drought conditions. Negative SPEI values indicate drier-than-normal conditions, with values below −1.0, −1.5, and −2.0 corresponding to moderate, severe, and extreme drought, respectively (McKee et al., 1993). Figure 25 presents the summer (JJA) mean SPEI series for all four timescales alongside the park-wide JJA-LST record, allowing direct comparison between drought conditions and surface temperature variability over the study period.

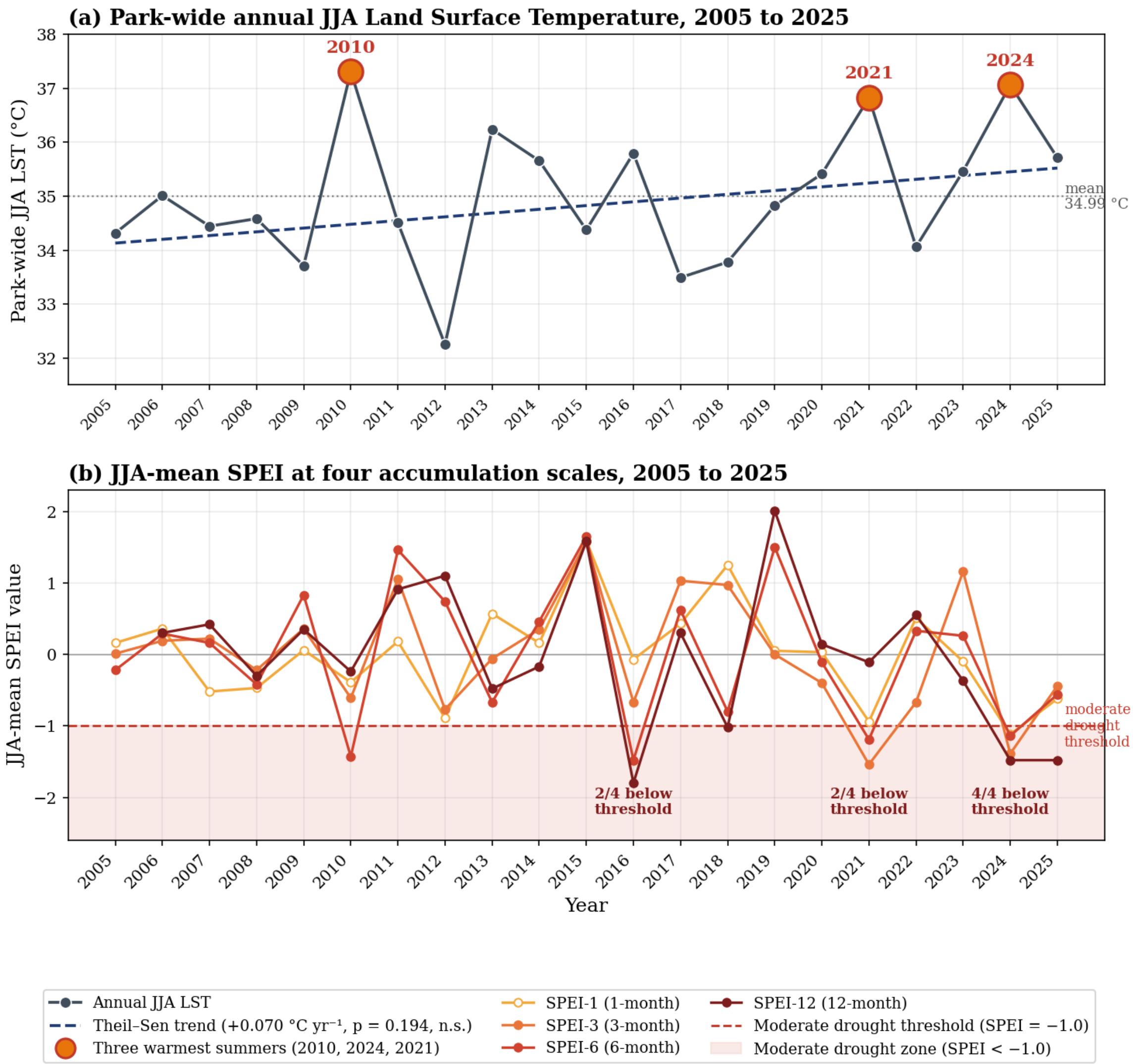

Figure 26. (a) Park-wide mean summer (JJA) Land Surface Temperature (LST) and (b) JJA mean Standardized Precipitation–Evapotranspiration Index (SPEI; 1-, 3-, 6-, and 12-month scales) from 2005 to 2025.

As shown in Figure 25a, the dashed line represents the Theil–Sen warming trend (+0.070 °C yr^{-1}; $p = 0.194$), while the dotted line indicates the 21-year mean summer LST (34.99 °C). The highlighted markers identify the three warmest summers in the record: 2010, 2024, and 2021. In Figure 25b, the dashed line marks the moderate drought threshold (SPEI = −1.0), and the shaded area represents drought conditions. Labels indicate the number of SPEI timescales that exceeded the drought threshold during each drought year (2/4 in 2016 and 2021, and 4/4 in 2024). Drought conditions varied across accumulation periods, indicating that drought developed at different temporal scales. At the short-term scale (SPEI-1), only 2024 reached moderate drought conditions. At the seasonal scale (SPEI-3), 2021 experienced severe drought (−1.54), while 2024 recorded moderate drought (−1.39). At the intermediate scale (SPEI-6), drought conditions occurred in 2010, 2016, 2021, and 2024, with 2016 and 2024 showing the greatest severity. At the annual scale (SPEI-12), severe drought was observed in 2016 (−1.80), moderate drought in 2018 (−1.02), and a prolonged drought period in 2024–2025 (both −1.48). Among these events, 2024 stands out as the only year in which all four

SPEI timescales simultaneously exceeded the drought threshold, representing a compound drought event that coincided with the second-warmest summer in the LST record. In contrast, 2016 was characterised by a severe long-term hydrological drought, while 2021 experienced the strongest seasonal drought signal. Together, the drought years identified by SPEI (2016, 2021, 2024, and 2025) provide the climatic context for interpreting subsequent patterns in LST, LAI dynamics, and their interactions.

6.6.4 Thermal Trajectory Segmentation of Land Surface Temperature.

At the pixel level (Figure 26a), LST dynamics were considerably more heterogeneous than those observed in the park-wide or plot-level analyses. Although many pixels exhibited no breakpoints and were characterized by a single temporal segment, breakpoints were common across the study area. Pixels with one or two breakpoints were widely distributed, while areas with a maximum of three breakpoints formed extensive clusters, particularly in the western and north-western sectors, the southern slopes, and along the eastern margin. This pattern indicates that local-scale temperature dynamics are more variable than aggregated park-level trends, where spatial averaging smooths year-to-year fluctuations. To complement the breakpoint analysis, the year of maximum annual warming was identified for each pixel from the fitted LandTrendr trajectory (Figure 26b). This represents the year with the largest year-to-year increase in LST. Because annual changes were calculated relative to the preceding year, the analysis covers the period 2006–2025, with 2005 excluded as a baseline year. The resulting map highlights the timing of the strongest warming events across the park and provides additional insight into the spatial distribution of thermal change.

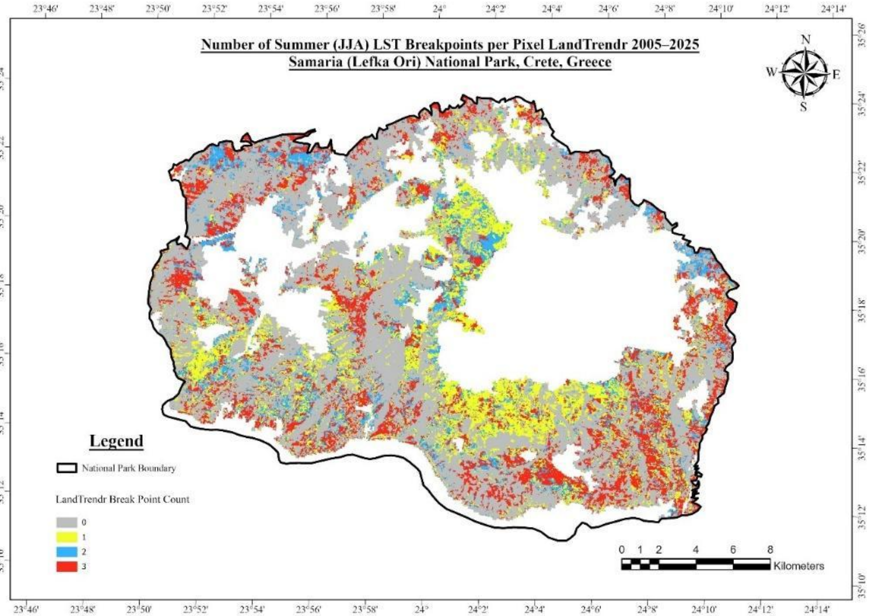

(a)

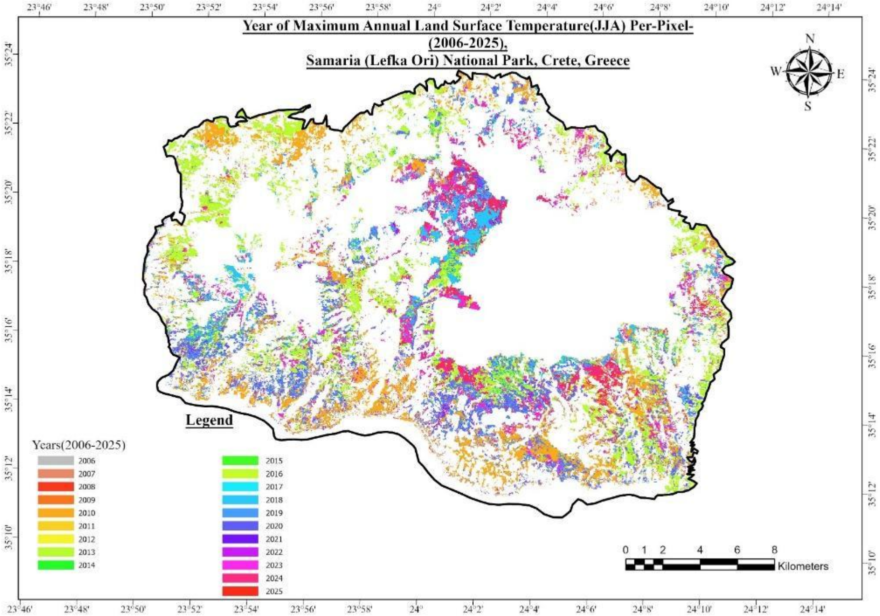

(b)

Figure 27. Number of LandTrendr breakpoints per pixel in the annual June-July-August Land Surface Temperature (JJA-LST) trajectory, 2005-2025 (a), and year of maximum annual land surface temperature for a pixel in the study area, 2006-2025 (b).

6.6.5 Leaf Area Index Variation across the Study Area and Plots

Mean summer (JJA) LAI across the study area was 0.50 $m^2\ m^{-2}$ during 2016–2025, with relatively low interannual variability (0.46–0.54 $m^2\ m^{-2}$). The highest LAI values were recorded in 2017 (0.538 $m^2\ m^{-2}$), 2025 (0.530 $m^2\ m^{-2}$), and 2023 (0.526 $m^2\ m^{-2}$), while the lowest occurred in 2016 (0.457 $m^2\ m^{-2}$), 2021 (0.481 $m^2\ m^{-2}$), and 2022 (0.485 $m^2\ m^{-2}$). A clear seasonal pattern was observed, with LAI decreasing from June (0.552 $m^2\ m^{-2}$) to July (0.503 $m^2\ m^{-2}$) and August (0.466 $m^2\ m^{-2}$), reflecting increasing water stress and seasonal senescence during the Mediterranean summer. Over the study period, LAI remained largely stable, with a Theil–Sen trend of +0.0019 $m^2\ m^{-2}\ yr^{-1}$ and a non-significant Mann–Kendall test result (τ = 0.07, p = 0.858). These findings indicate no detectable long-term change in summer vegetation density between 2016 and 2025. It should be noted that these estimates represent averages across all vegetation classes included in the analysis, namely coniferous forest, natural grassland, and transitional woodland-shrub.

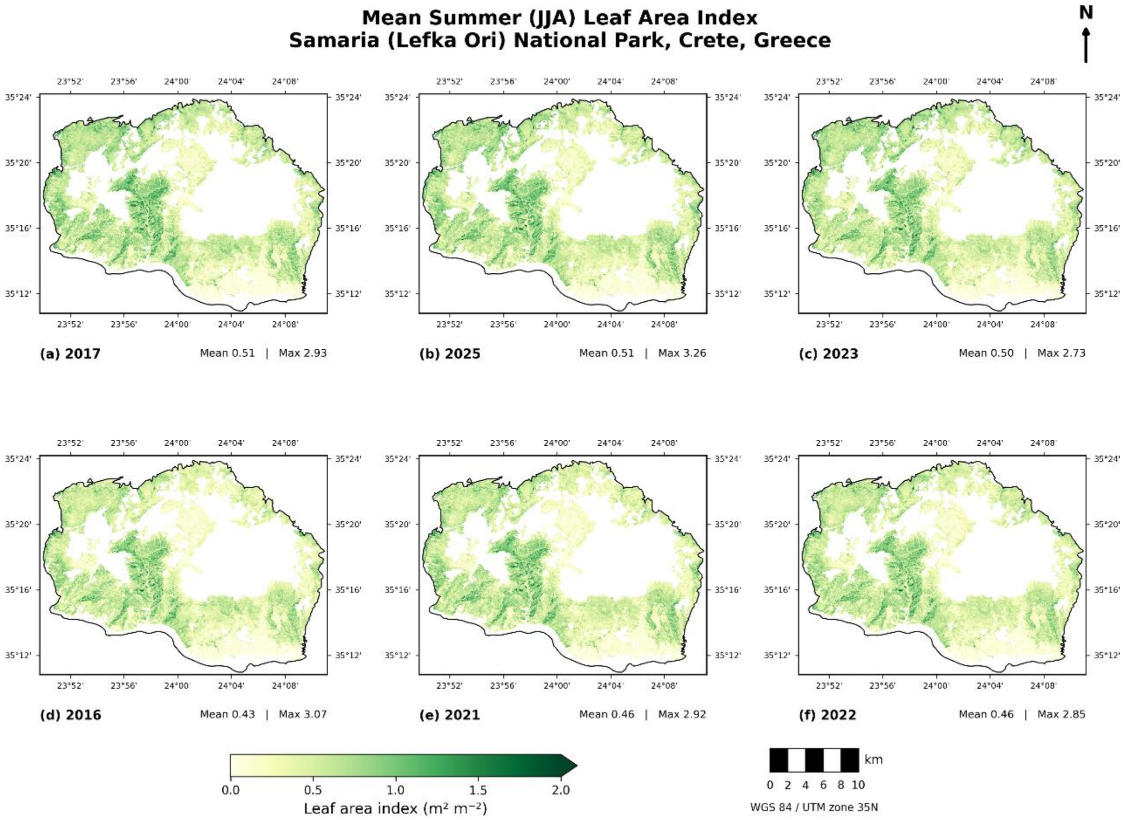

Figure 28. Summer (i.e., June, July, and August) leaf area index (JJA-LAI) in selected years showing (a-c) higher-LAI years (2017, 2025, and 2023) and (d-f) lower-LAI years (2016, 2021, and 2022).

At the plot level, mean summer (JJA) LAI ranged from 0.07 to 0.45 $m^2\ m^{-2}$ (mean = 0.30 $m^2\ m^{-2}$), reflecting the open and sparsely vegetated Calabrian pine stands sampled in the field. The highest values were observed at Plots 16, 2, and 5, while the lowest occurred at Plots 13, 7, and 9. Plot 13 consistently exhibited near-zero LAI, indicating very sparse vegetation cover. Trend analysis revealed no significant changes in LAI between 2016 and 2025. Although three plots were significant at the uncorrected $p < 0.05$ level, none remained significant after Benjamini–Hochberg correction. Overall, LAI remained stable across the plot network throughout the study period.

6.6.6 Land Surface Temperature–Leaf Area Index Coupling

The relationship between thermal stress and vegetation condition was evaluated across the 29 field plots using plot-level anomaly time series. By removing static differences in elevation, aspect, and canopy density, the analysis focused on temporal variations in LST and LAI. Evidence was drawn from trend analysis, thermal gradient analysis, and LST–LAI relationships across multiple temporal scales. Mann–Kendall trend analysis detected significant warming in 28 of the 29 plots, confirming the widespread increase in summer LST across the study area. In contrast, LAI remained largely stable, with significant trends observed in only three plots and a small positive median Theil–Sen slope.

When the thermal environment was analysed as a continuous gradient, mean LAI declined significantly with increasing mean summer LST (OLS slope = -0.031 $m^2\ m^{-2}\ °C^{-1}$, $R^2 = 0.15$, $p = 0.037$; Spearman $\rho = -0.34$, $p = 0.075$). This indicates that warmer plots generally supported sparser canopies. However, neither LAI trends nor interannual variability was significantly related to mean LST or warming rate, and mixed-effects modelling showed no evidence that hotter plots experienced faster canopy decline over time ($p = 0.88$). Thus, the observed relationship reflects a stable spatial pattern rather than progressive divergence among plots. Interannual correlation analysis revealed a significant negative relationship between summer LST and LAI in the same year (lag 0: $r = -0.235$, $p = 0.0006$; Figure 29), indicating that warmer summers were associated with reduced canopy density. This pattern remained significant after AR(1) pre-whitening ($r = -0.22$, $p = 0.004$), confirming that it was not driven by temporal autocorrelation. Relationships at one- and two-year lags were weak and generally non-significant, suggesting limited long-term carryover effects and partial canopy recovery following warm years. Although a strong negative correlation was observed at the three-year lag ($r = -0.57$), this result is based on a small sample size and should be interpreted with caution.

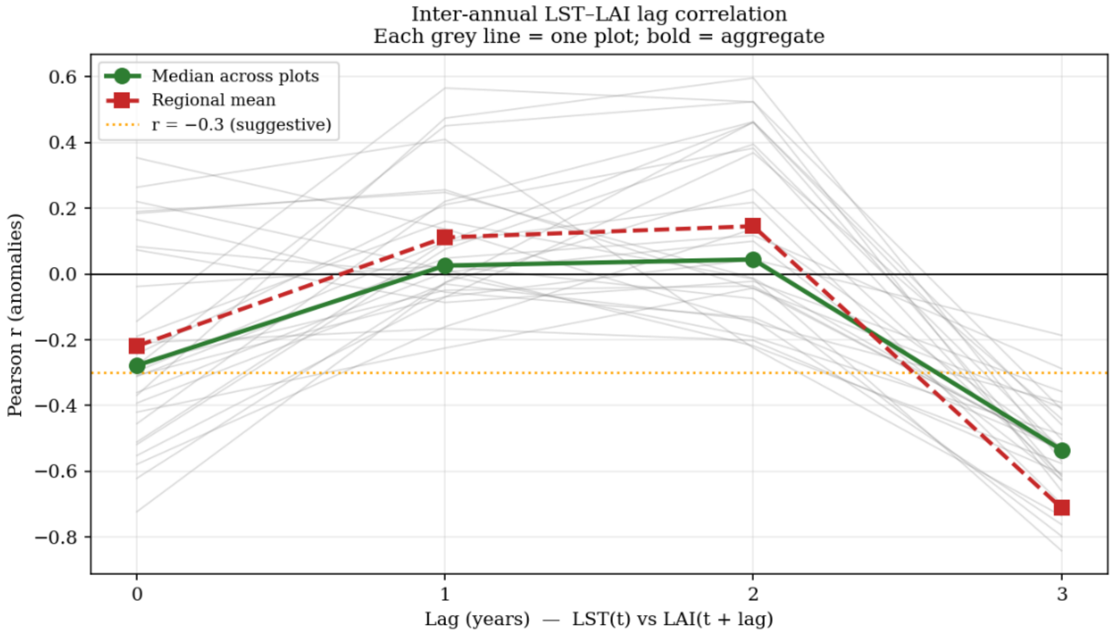

Figure 29. Interannual Land Surface Temperature-Leaf Area Index (LST-LAI) lag correlation based on leave-one-out anomaly time series.

Monthly analyses produced a similar but weaker pattern (Figure 30), with a modest negative same-year relationship (r = −0.14), a weak positive response after one year (r = +0.12), and renewed negative coupling after three years (r = −0.16). Significant responses were detected in only a few individual plots, indicating that the LST–LAI relationship is relatively weak at the plot scale. Overall, the monthly analysis supported the annual results but did not reveal additional patterns.

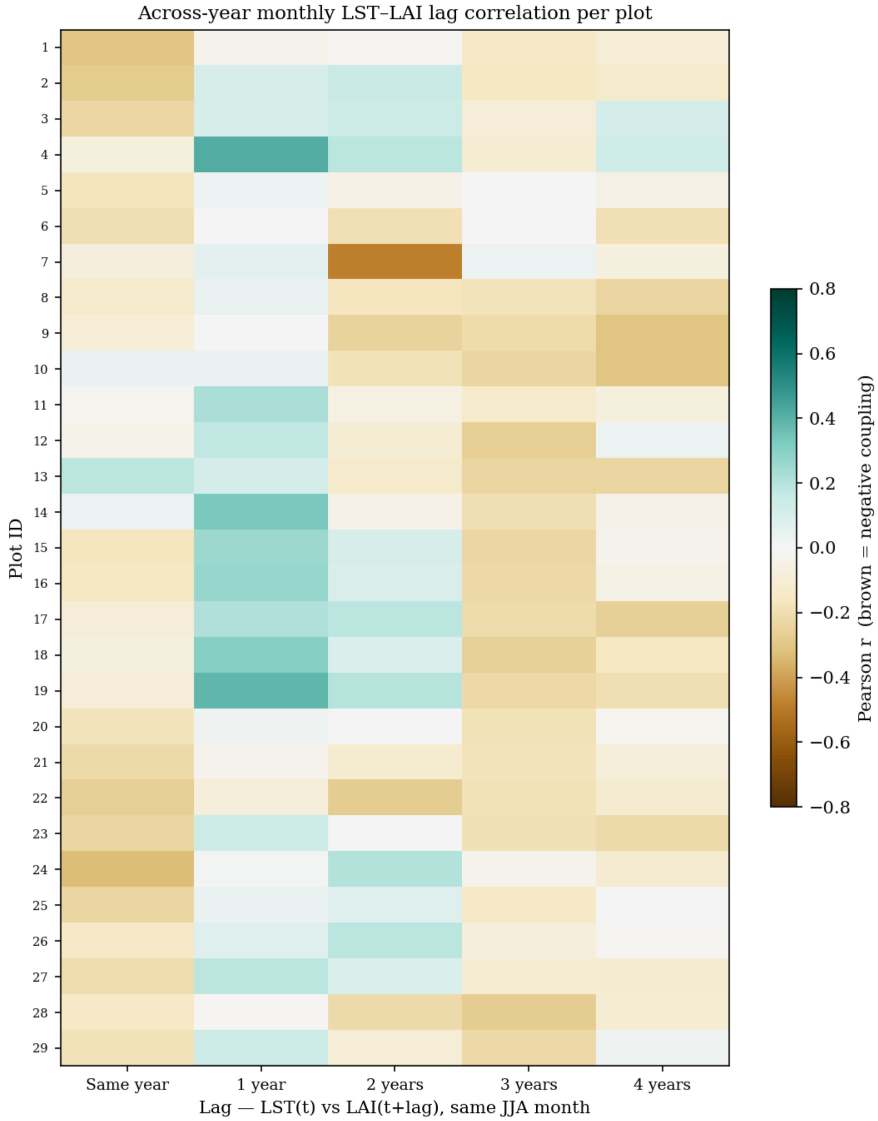

Figure 30. Across-year monthly land surface temperature-leaf area index (LST-LAI) lag correlation per plot.

The results revealed that summer LST exhibited a stable, topographically driven north–south gradient, with persistent hotspots concentrated along the lower southern margin and cooler conditions in the higher northern interior. Although the park-wide warming trend was positive (+0.070 °C yr^{-1}), it was not statistically significant. Nevertheless, several plots within the southern hotspot belt showed significant warming (median +0.244 °C yr^{-1}). LST responded strongly to drought, increasing by approximately 1.8 °C during drought summers and showing the strongest relationship with SPEI-6 ($r = -0.63$), although these effects were largely transient, with temperatures returning to baseline in subsequent years.

The relationship between LST and LAI was consistently negative across spatial and temporal scales, supporting the hypothesis that warmer conditions are associated with lower leaf area. However, canopy responses appeared reversible, with LAI recovering following drought events and showing no long-term decline despite two decades of warming.

The open Calabrian pine forest of Samaria National Park appears thermally sensitive yet resilient. Both surface temperature and canopy condition respond to drought-driven heat stress but recover when moisture availability improves. The persistent southern hotspot belt represents the most vulnerable area of the park and should remain a priority for long-term monitoring. While no sustained decline in canopy condition was detected during the study period, continued observation is needed to assess whether this resilience can be maintained under future climate warming.

6.7 Distribution of the Products

All generated products were uploaded to and stored in the DNAS platform, which serves as the central repository for the ITC EO products, metadata, and associated documentation. The platform ensures standardised data management, secure storage, and controlled access in accordance with the project's Data Management Plan. The products are currently under review by DANS services.

For LAI generated products: https://doi.org/10.17026/PT/QCQ9C3

For LST-generated products: https://doi.org/10.17026/PT/RJYTYO

7 References

[1] Aalto, J., Lehtonen, I., Pirinen, P., Aapala, K., Heikkinen, R.K., 2023. Bioclimate change across the protected area network of Finland. Science of The Total Environment 893, 164782.

[2] Abdullah, H., Neinavaz, E., Darvishzadeh, R., Huesca, M., Skidmore, A. K., Lindeskog, M., Smith, B., Heurich, M., Steinbrecher, R., & Paganini, M. (2025). Integrating process-based vegetation modelling with high-resolution imagery to assess bark beetle infestation and land surface temperature effects on forest net primary productivity. *Remote Sensing Applications: Society and Environment, 37*, Article 101499. https://doi.org/10.1016/j.rsase.2025.101499

[3] Assessment of vegetation composition at model sites in the Vysočina Region. Internal case-study report, 2026.

[4] Beguería, S., Vicente-Serrano, S. M., Reig, F., & Latorre, B. (2014). Standardized precipitation evapotranspiration index (SPEI) revisited: Parameter fitting, evapotranspiration models, tools, datasets and drought monitoring. *International Journal of Climatology, 34*(10), 3001–3023. https://doi.org/10.1002/joc.3887

[5] Benjamini, Y., & Hochberg, Y. (1995). Controlling the false discovery rate: A practical and powerful approach to multiple testing. *Journal of the Royal Statistical Society: Series B (Methodological), 57*(1), 289–300. https://doi.org/10.1111/j.2517-6161.1995.tb02031.x

[6] Bento, V. A., Gouveia, C. M., DaCamara, C. C., Trigo, I. F., & Libonati, R. (2020). The roles of NDVI and land surface temperature when using the Vegetation Health Index over dry regions. *Global and Planetary Change, 190*, Article 103198. https://doi.org/10.1016/j.gloplacha.2020.103198

[7] Bonari, G., Fernández-González, F., Çoban, S., Monteiro-Henriques, T., Bergmeier, E., Didukh, Y. P., Xystrakis, F., Angiolini, C., Chytrý, K., & Chytrý, M. (2021). Classification of the Mediterranean lowland to submontane pine forest vegetation. *Applied Vegetation Science, 24*(1), Article e12544. https://doi.org/10.1111/avsc.12544

[8] Boteva, D., Griffiths, G., & Dimopoulos, P. (2004). Evaluation and mapping of the conservation significance of habitats using GIS: An example from Crete, Greece. *Journal for Nature Conservation, 12*(4), 237–250. https://doi.org/10.1016/j.jnc.2004.09.002

[9] Böttcher, K. (2025). Start of vegetation period in coniferous and deciduous forests (phenology). Finnish Environment Institute. Data available from: https://www.syke.fi/en/environmental-data/downloadable-spatial-datasets#start-vegetation-period-coniferous-and-deciduous-forests-phenology.

[10] Böttcher, K., Markkanen, T., Thum, T., Aalto, T., Aurela, M., Reick, C., Kolari, P., Arslan, A., Pulliainen, J., 2016. Evaluating biosphere model estimates of the start of the vegetation active season in boreal forests by satellite observations. Remote Sensing 8, 580.

[11] Chicco, D., Warrens, M. J., & Jurman, G. (2021). The coefficient of determination R-squared is more informative than SMAPE, MAE, MAPE, MSE and RMSE in regression analysis evaluation. *PeerJ Computer Science, 7*, Article e623. https://doi.org/10.7717/peerj-cs.623

[12] Ciais, P., Reichstein, M., Viovy, N., Granier, A., Ogée, J., Allard, V., Aubinet, M., Buchmann, N., Bernhofer, C., Carrara, A., Chevallier, F., De Noblet, N., Friend, A. D., Friedlingstein, P., Grünwald, T., Heinesch, B., Keronen, P., Knohl, A., Krinner, G., … Valentini, R. (2005). Europe-wide reduction in primary productivity caused by the heat and drought in 2003. *Nature, 437*(7058), 529–533. https://doi.org/10.1038/nature03972

[13] Clark, J. S., Iverson, L., Woodall, C. W., Allen, C. D., Bell, D. M., Bragg, D. C., D'Amato, A. W., Davis, F. W., Hersh, M. H., Ibáñez, I., Jackson, S. T., Matthews, S., Pederson, N., Peters, M., Schwartz, M. W., Waring, K. M., & Zimmermann, N. E. (2016). The impacts of increasing drought on forest dynamics, structure, and biodiversity in the United States. *Global Change Biology, 22*(7), 2329–2352. https://doi.org/10.1111/gcb.13160

[14] Clevers, J. G. P. W., Kooistra, L., & van den Brande, M. M. M. (2017). Using Sentinel-2 data for retrieving LAI and leaf and canopy chlorophyll content of a potato crop. *Remote Sensing, 9*(5), Article 405. https://doi.org/10.3390/rs9050405

[15] Copernicus Land Monitoring Service (CLMS) (2021). High Resolution Vegetation Phenology and Productivity (HR-VPP) – Seasonal Productivity 2017–present (10 m), Europe, version 1. European Environment Agency (EEA). https://doi.org/10.2909/5ae0f2a2-7ad8-4f7c-878d-f1b09d78d7a1.

[16] Copernicus/ESA. Sentinel-2 User Handbook and Copernicus Data Space documentation for B4 red and B8 near-infrared observations.

[17] Danopoulos, A., Tsaliki, E., & Kontoes, C. (2022). Time series analysis of Landsat data for investigating the relationship between land surface temperature and forest changes in Paphos forest, Cyprus. *Remote Sensing, 14*(4), Article 1010. https://doi.org/10.3390/rs14041010

[18] Eliades, M., Bruggeman, A., Lubczynski, M. W., Christou, A., Camera, C., & Djuma, H. (2018). The water balance components of Mediterranean pine trees on a steep mountain slope during two hydrologically contrasting years. *Journal of Hydrology, 562*, 712–724. https://doi.org/10.1016/j.jhydrol.2018.05.048

[19] European Environment Agency. (2020). *CORINE Land Cover 2018 (raster 100 m), Europe, 6-yearly — version 2020_20u1* [Data set]. Copernicus Land Monitoring Service. https://doi.org/10.2909/960998c1-1870-4e82-8051-6485205ebbac

[20] Finnish Environment Institute (2024). Harmonized Landsat satellite image mosaic timeseries. https://ckan.ymparisto.fi//dataset/%7B77365632-A3BD-4ADA-A699-3A7847E35B24%7D. Data available at: https://nsdc.fmi.fi/.

[21] Fu, Z., Ciais, P., Bastos, A., Stoy, P. C., Yang, H., Green, J. K., Wang, B., Yu, K., Huang, Y., Knohl, A., Sigut, L., Gharun, M., Cuntz, M., Arriga, N., Roland, M., Peichl, M., Migliavacca, M., Cremonese, E., Varlagin, A., & Koebsch, F. (2020). Sensitivity of gross primary productivity to climatic drivers during the summer drought of 2018 in Europe. *Philosophical Transactions of the Royal Society B: Biological Sciences, 375*(1810), Article 20190747. https://doi.org/10.1098/rstb.2019.0747

[22] GEO BON. EBV classes and Ecosystem Function Working Group: ecosystem phenology, primary productivity, and ecosystem disturbance as ecosystem-functioning EBVs.

[23] Georghiou, K., & Delipetrou, P. (2010). Patterns and traits of the endemic plants of Greece. *Botanical Journal of the Linnean Society, 162*(2), 130–153. https://doi.org/10.1111/j.1095-8339.2010.01025.x

[24] Getis, A., & Ord, J. K. (1992). The analysis of spatial association by use of distance statistics. *Geographical Analysis, 24*(3), 189–206. https://doi.org/10.1111/j.1538-4632.1992.tb00261.x

[25] Global Climate Observing System (GCOS). Essential Climate Variable: Land Surface Temperature.

[26] Gringorten, I. I. (1963). A plotting rule for extreme probability paper. *Journal of Geophysical Research, 68*(3), 813–814. https://doi.org/10.1029/JZ068i003p00813

[27] Guion, A., Turquety, S., Polcher, J., Pennel, R., Bastin, S., & Arsouze, T. (2022). Droughts and heatwaves in the Western Mediterranean: Impact on vegetation and wildfires using the coupled WRF–ORCHIDEE regional model (RegIPSL). Climate Dynamics, 58, 2881–2903. https://doi.org/10.1007/s00382-021-05938-y

[28] Haied, N., Foufou, A., Khadri, S., Boussaid, A., Azlaoui, M., & Bougherira, N. (2023). Spatial and temporal assessment of drought hazard, vulnerability and risk in three different climatic zones in Algeria. *Sustainability, 15*(10), Article 7803. https://doi.org/10.3390/su15107803

[29] Hao, Z., & AghaKouchak, A. (2014). A nonparametric multivariate multi-index drought monitoring framework. *Journal of Hydrometeorology, 15*(1), 89–101. https://doi.org/10.1175/JHM-D-12-0160.1

[30] Huete, A., Didan, K., Miura, T., Rodriguez, E. P., Gao, X., & Ferreira, L. G. (2002). Overview of the radiometric and biophysical performance of the MODIS vegetation indices. *Remote Sensing of Environment, 83*(1–2), 195–213. https://doi.org/10.1016/S0034-4257(02)00096-2

[31] Intergovernmental Panel on Climate Change. (2023). *Climate change 2022 – Impacts, adaptation and vulnerability: Working Group II contribution to the Sixth Assessment Report of the Intergovernmental Panel on Climate Change* (1st ed.). Cambridge University Press. https://doi.org/10.1017/9781009325844

[32] Italiano, S. S. P., Gazol, A., Camarero, J. J., & Colangelo, M. (2023). Radial growth, wood anatomical traits and remote sensing indexes reflect different impacts of drought on Mediterranean forests. *Forest Ecology and Management, 546*, Article 121334. https://doi.org/10.1016/j.foreco.2023.121334

[33] Jedlička, K., et al., 2021. Calculation of agro-climatic factors from global climatic data. Applied Sciences 11(3), 1245.

[34] Jiménez-Muñoz, J. C., & Sobrino, J. A. (2003). A generalized single-channel method for retrieving land surface temperature from remote sensing data. *Journal of Geophysical Research: Atmospheres, 108*(D22), Article 4688. https://doi.org/10.1029/2003JD003480

[35] Jonckheere, I., Nackaerts, K., Muys, B., & Coppin, P. (2005). Assessment of automatic gap fraction estimation of forests from digital hemispherical photography. *Agricultural and Forest Meteorology, 132*(1–2), 96–114. https://doi.org/10.1016/j.agrformet.2005.06.003

[36] Juha, A., & Pentti, P. (2023). Bioclimate change across the protected area network of Finland (Version 1). Finnish Meteorological Institute. https://doi.org/10.23728/fmi-b2share.0cf61af0801f4bf3a9d1336fcbbd324e.

[37] Karinou, F., Agathangelidis, I., & Cartalis, C. (2025). Assessing the combined impact of land surface temperature and droughts to heatwaves over Europe between 2003 and 2023. *Remote Sensing, 17*(9), Article 1655. https://doi.org/10.3390/rs17091655

[38] Kennedy, R. E., Yang, Z., & Cohen, W. B. (2010). Detecting trends in forest disturbance and recovery using yearly Landsat time series: 1. LandTrendr — Temporal segmentation algorithms. *Remote Sensing of Environment, 114*(12), 2897–2910. https://doi.org/10.1016/j.rse.2010.07.008

[39] Kennedy, R. E., Yang, Z., Gorelick, N., Braaten, J., Cavalcante, L., Cohen, W. B., & Healey, S. (2018). Implementation of the LandTrendr algorithm on Google Earth Engine. *Remote Sensing, 10*(5), Article 691. https://doi.org/10.3390/rs10050691

[40] Kliengchuay, W., Phonphan, W., Niampradit, S., Kiangkoo, N., Srimanus, W., Niemmanee, T., Arunplod, C., Wen, B., Guo, Y., Herbreteau, V., & Tantrakarnapa, K. (2025). Variation of vegetation cover and the relationship with land surface temperature across Thailand (2007 to 2022). *Scientific Reports, 15*(1), Article 27823. https://doi.org/10.1038/s41598-025-13018-y

[41] Kosmas, C., Kirkby, M., & Geeson, N. (Eds.). (1999). *The MEDALUS project: Mediterranean desertification and land use. Manual on key indicators of desertification and mapping environmentally sensitive areas to desertification* (EUR 18882). European Commission.

[42] Kougioumoutzis, K., Kokkoris, I. P., Panitsa, M., Trigas, P., Strid, A., & Dimopoulos, P. (2020). Plant diversity patterns and conservation implications under climate-change scenarios in the Mediterranean: The case of Crete (Aegean, Greece). *Diversity, 12*(7), Article 270. https://doi.org/10.3390/d12070270

[43] Kvålseth, T. O. (1985). Cautionary note about R2. *The American Statistician, 39*(4), 279–285. https://doi.org/10.1080/00031305.1985.10479448

[44] Lawlor, D. W., & Cornic, G. (2002). Photosynthetic carbon assimilation and associated metabolism in relation to water deficits in higher plants. *Plant, Cell & Environment, 25*(2), 275–294. https://doi.org/10.1046/j.0016-8025.2001.00814.x

[45] Li, Z.-L., Leng, P., Zhou, C., Chen, K.-S., Zhou, F.-C., & Shang, G.-F. (2023). Satellite remote sensing of global land surface temperature: Definition, methods, products, and applications. *Reviews of Geophysics, 61*(1), Article e2022RG000777. https://doi.org/10.1029/2022RG000777

[46] Macfarlane, C., Hoffman, M., Eamus, D., Kerp, N., Higginson, S., McMurtrie, R., & Adams, M. (2007). Estimation of leaf area index in eucalypt forest using digital photography. *Agricultural and Forest Meteorology, 143*(3–4), 176–188. https://doi.org/10.1016/j.agrformet.2006.10.013

[47] Mann, H. B. (1945). Nonparametric tests against trend. *Econometrica, 13*(3), 245–259. https://doi.org/10.2307/1907187

[48] Manoutsoglou, E., Lazos, I., Steiakakis, E., & Vafeidis, A. (2022). The geomorphological and geological structure of the Samaria Gorge, Crete, Greece. *Applied Sciences, 12*(20), Article 10670. https://doi.org/10.3390/app122010670

[49] McKee, T. B., Doesken, N. J., & Kleist, J. (1993). The relationship of drought frequency and duration to time scales. In *Proceedings of the 8th Conference on Applied Climatology* (pp. 179–184). American Meteorological Society.

[50] Metsämäki, S. (2025). Yearly European Melt-off-day (2001–2023) (Version 1). Finnish Environment Institute. https://doi.org/10.23729/fd-1bad8a16-9edf-38d9-9628-2bd025d8d9ce.

[51] Metsämäki, S., Böttcher, K., Pulliainen, J., Luojus, K., Cohen, J., Takala, M., Mattila, O.-P., Schwaizer, G., Derksen, C., Koponen, S., 2018. The accuracy of snow melt-off day derived from optical and microwave radiometer data—A study for Europe. Remote Sensing of Environment 211, 1–12.

[52] Morianou, G. G., Kourgialas, N. N., Psarras, G., & Koubouris, G. C. (2018). Mapping sensitivity to desertification in Crete (Greece), the risk for agricultural areas. *Journal of Water and Climate Change, 9*(4), 691–702. https://doi.org/10.2166/wcc.2018.148

BioClima

[53] Muñoz-Sabater, J. (2019). *ERA5-Land monthly averaged data from 1981 to present* [Data set]. Copernicus Climate Change Service (C3S) Climate Data Store. https://doi.org/10.24381/cds.68d2bb30

[54] Muñoz-Sabater, J., Dutra, E., Agustí-Panareda, A., Albergel, C., Arduini, G., Balsamo, G., Boussetta, S., Choulga, M., Harrigan, S., Hersbach, H., Martens, B., Miralles, D. G., Piles, M., Rodríguez-Fernández, N. J., Zsoter, E., Buontempo, C., & Thépaut, J.-N. (2021). ERA5-Land: A state-of-the-art global reanalysis dataset for land applications. *Earth System Science Data, 13*(9), 4349–4383. https://doi.org/10.5194/essd-13-4349-2021

[55] Neinavaz, E., Skidmore, A. K., & Darvishzadeh, R. (2020). Effects of prediction accuracy of the proportion of vegetation cover on land surface emissivity and temperature using the NDVI threshold method. *International Journal of Applied Earth Observation and Geoinformation, 85*, Article 101984. https://doi.org/10.1016/j.jag.2019.101984

[56] Ord, J. K., & Getis, A. (1995). Local spatial autocorrelation statistics: Distributional issues and an application. *Geographical Analysis, 27*(4), 286–306. https://doi.org/10.1111/j.1538-4632.1995.tb00912.x

[57] Perkins, S. E., & Alexander, L. V. (2013). On the measurement of heat waves. *Journal of Climate, 26*(13), 4500–4517. https://doi.org/10.1175/JCLI-D-12-00383.1

[58] Qiao, M., Hong, C., Jiao, Y., Hou, S., & Gao, H. (2024). Impacts of drought on photosynthesis in major food crops and the related mechanisms of plant responses to drought. *Plants, 13*(13), Article 1808. https://doi.org/10.3390/plants13131808

[59] Pulliainen, J., Luojus, K., Derksen, C., Mudryk, L., Lemmetyinen, J., Salminen, M., Ikonen, J., Takala, M., Cohen, J., Smolander, T., Norberg, J., 2020. Patterns and trends of Northern Hemisphere snow mass from 1980 to 2018. Nature 581, 294–298.

[60] Rakovec, O., Samaniego, L., Hari, V., Markonis, Y., Moravec, V., Thober, S., Hanel, M., & Kumar, R. (2022). The 2018–2020 multi-year drought sets a new benchmark in Europe. *Earth's Future, 10*(3), Article e2021EF002394. https://doi.org/10.1029/2021EF002394

[61] Rantanen, M., Karpechko, A.Y., Lipponen, A., Nordling, K., Hyvärinen, O., Ruosteenoja, K., Vihma, T., Laaksonen, A., 2022. The Arctic has warmed nearly four times faster than the globe since 1979. Communications Earth & Environment 3, 168.

[62] Rozenstein, O., Qin, Z., Derimian, Y., & Karnieli, A. (2014). Derivation of land surface temperature for Landsat-8 TIRS using a split window algorithm. *Sensors, 14*(4), 5768–5780. https://doi.org/10.3390/s140405768

[63] Russo, D., Marziliano, P. A., Macrì, G., Zimbalatti, G., Tognetti, R., & Lombardi, F. (2019). Tree growth and wood quality in pure vs. mixed-species stands of European beech and Calabrian pine in Mediterranean mountain forests. *Forests, 11*(1), Article 6. https://doi.org/10.3390/f11010006

[64] Sabater, S., Freixa, A., Jiménez, L., López-Doval, J., Pace, G., Pascoal, C., Perujo, N., Craven, D., & González-Trujillo, J. D. (2023). Extreme weather events threaten biodiversity and functions of river ecosystems: Evidence from a meta-analysis. *Biological Reviews, 98*(2), 450–461. https://doi.org/10.1111/brv.12914

[65] Sebastiani, A., Manes, F., & Salvatori, E. (2023). Comparing leaf area index estimates in a Mediterranean forest using field measurements, Landsat 8, and Sentinel-2 data. *Ecological Processes, 12*, Article 34. https://doi.org/10.1186/s13717-023-00441-0

[66] Sobrino, J. A., Jiménez-Muñoz, J. C., & Paolini, L. (2004). Land surface temperature retrieval from LANDSAT TM 5. *Remote Sensing of Environment, 90*(4), 434–440. https://doi.org/10.1016/j.rse.2004.02.003

[67] Solano, F., Mansi, C., Baliva, M., Canestrelli, D., Chiarucci, A., Manicone, R., Maugeri, M., Modica, G., Palli, J., Quilghini, G., & Piovesan, G. (2025). Mediterranean strictly protected forests are cooler. *Agricultural and Forest Meteorology, 375*, Article 110858. https://doi.org/10.1016/j.agrformet.2025.110858

[68] Stagge, J. H., Tallaksen, L. M., Gudmundsson, L., Van Loon, A. F., & Stahl, K. (2015). Candidate distributions for climatological drought indices (SPI and SPEI). *International Journal of Climatology, 35*(13), 4027–4040. https://doi.org/10.1002/joc.4267

[69] Stobbelaar, P., Neinavaz, E., & Nyktas, P. (2022). Prediction of leaf area index using thermal infrared data acquired by UAS over a mixed temperate forest. *International Journal of Applied Earth Observation and Geoinformation, 114*, Article 103049. https://doi.org/10.1016/j.jag.2022.103049

[70] Tammilehto, A., Härmä, P., Kallio, M., Törmä, M., Saikkonen, A., Tuominen, S., Impiö, M., Heikkinen, M., Kervinen, M., Jussila, T., Böttcher, K., Pääkkö, E., Kokko, A., Mäkelä, K., Anttila, S., 2024. Ylä-Lapin luonnon kaukokartoitus, Projektin loppuraportti osa 1 – Aineistot ja menetelmät (Remote sensing the habitats of Northern Lapland – Final project report part 1 – Materials and methods). Metsähallitus Luonnonsuojelujulkaisuja Sarja A, p. 103. Available online: https://julkaisut.metsa.fi/wp-content/uploads/sites/2/2024/02/a248.pdf (accessed 20.08.2024).

[71] Teskey, R., Wertin, T., Bauweraerts, I., Ameye, M., McGuire, M. A., & Steppe, K. (2015). Responses of tree species to heat waves and extreme heat events. *Plant, Cell & Environment, 38*(9), 1699–1712. https://doi.org/10.1111/pce.12417

[72] Theil, H. (1950). A rank-invariant method of linear and polynomial regression analysis. *Proceedings of the Royal Netherlands Academy of Sciences (KNAW), 53*, 386–392, 521–525, 1397–1412.

[73] Thornthwaite, C. W. (1948). An approach toward a rational classification of climate. *Geographical Review, 38*(1), 55–94. https://doi.org/10.2307/210739

[74] U.S. Geological Survey. Landsat Collection 2 Level-2 Surface Temperature product and scaling guidance.

[75] United Nations Convention to Combat Desertification. (1994). *United Nations Convention to Combat Desertification in those countries experiencing serious drought and/or desertification, particularly in Africa*. United Nations.

[76] VŠÚO Holovousy. Result sheet VL732: determination of soil pH, mineral nitrogen, mineral composition, and heavy metals. Issued 21 May 2026.

[77] Van Der Molen, M. K., Dolman, A. J., Ciais, P., Eglin, T., Gobron, N., Law, B. E., Meir, P., Peters, W., Phillips, O. L., Reichstein, M., Chen, T., Dekker, S. C., Doubková, M., Friedl, M. A., Jung, M., Van Den Hurk, B. J. J. M., De Jeu, R. A. M., Kruijt, B., Ohta, T., & Wang, G. (2011). Drought and ecosystem carbon cycling. *Agricultural and Forest Meteorology, 151*(7), 765–773. https://doi.org/10.1016/j.agrformet.2011.01.018

[78] Vicente-Serrano, S. M., Beguería, S., & López-Moreno, J. I. (2010). A multiscalar drought index sensitive to global warming: The standardized precipitation evapotranspiration index. *Journal of Climate, 23*(7), 1696–1718. https://doi.org/10.1175/2009JCLI2909.1

[79] Vogiatzakis, I. N., Mannion, A. M., & Griffiths, G. H. (2006). Mediterranean ecosystems: Problems and tools for conservation. *Progress in Physical Geography: Earth and Environment, 30*(2), 175–200. https://doi.org/10.1191/0309133306pp472ra

[80] Wilhite, D. A., Sivakumar, M. V. K., & Pulwarty, R. (2014). Managing drought risk in a changing climate: The role of national drought policy. *Weather and Climate Extremes, 3*, 4–13. https://doi.org/10.1016/j.wace.2014.01.002

[81] Yang, Q., Jiang, C., & Ding, T. (2023). Impacts of extreme-high-temperature events on vegetation in North China. *Remote Sensing, 15*(18), Article 4542. https://doi.org/10.3390/rs15184542

[82] Yin, J., Gentine, P., Slater, L., Gu, L., Pokhrel, Y., Hanasaki, N., Guo, S., Xiong, L., & Schlenker, W. (2023). Future socio-ecosystem productivity threatened by compound drought–heatwave events. *Nature Sustainability, 6*(3), 259–272. https://doi.org/10.1038/s41893-022-01024-1

[83] Yue, S., Pilon, P., Phinney, B., & Cavadias, G. (2002). The influence of autocorrelation on the ability to detect trend in hydrological series. *Hydrological Processes, 16*(9), 1807–1829. https://doi.org/10.1002/hyp.109